materials

MDPI

Review

Ga_2O_3 and Related Ultra-Wide Bandgap Power Semiconductor Oxides: New Energy Electronics Solutions for CO_2 Emission Mitigation

Zeyu Chi [1,†], Jacob J. Asher [2,†], Michael R. Jennings [2], Ekaterine Chikoidze [1] and Amador Pérez-Tomás [3,*]

[1] Groupe d'Etude de la Matière Condensée (GEMaC), UVSQ-CNRS, Université Paris-Saclay, 45 Av. des Etats-Unis, CEDEX, 78035 Versailles, France; zeyu.chi@uvsq.fr (Z.C.); ekaterine.chikoidze@uvsq.fr (E.C.)
[2] Bay Campus, College of Engineering, Swansea University, Fabian Way, Crymlyn Burrows, Swansea SA1 8EN, UK; j.j.asher.796600@swansea.ac.uk (J.J.A.); m.r.jennings@swansea.ac.uk (M.R.J.)
[3] Catalan Institute of Nanoscience and Nanotechnology (ICN2), CSIC and BIST, Campus UAB, Bellaterra, 08193 Barcelona, Spain
* Correspondence: amador.perez@icn2.cat
† These authors contributed equally to this work.

Abstract: Currently, a significant portion (~50%) of global warming emissions, such as CO_2, are related to energy production and transportation. As most energy usage will be electrical (as well as transportation), the efficient management of electrical power is thus central to achieve the XXI century climatic goals. Ultra-wide bandgap (UWBG) semiconductors are at the very frontier of electronics for energy management or energy electronics. A new generation of UWBG semiconductors will open new territories for higher power rated power electronics and solar-blind deeper ultraviolet optoelectronics. Gallium oxide—Ga_2O_3 (4.5–4.9 eV), has recently emerged pushing the limits set by more conventional WBG (~3 eV) materials, such as SiC and GaN, as well as for transparent conducting oxides (TCO), such asIn_2O_3, ZnO and SnO_2, to name a few. Indeed, Ga_2O_3 as the first oxide used as a semiconductor for power electronics, has sparked an interest in oxide semiconductors to be investigated (oxides represent the largest family of UWBG). Among these new power electronic materials, $Al_xGa_{1-x}O_3$ may provide high-power heterostructure electronic and photonic devices at bandgaps far beyond all materials available today (~8 eV) or $ZnGa_2O_4$ (~5 eV), enabling spinel bipolar energy electronics for the first time ever. Here, we review the state-of-the-art and prospects of some ultra-wide bandgap oxide semiconductor arising technologies as promising innovative material solutions towards a sustainable zero emission society.

Keywords: energy electronics; ultra-wide bandgap; power electronics; diodes; transistors; gallium oxide; Ga_2O_3; spinel; $ZnGa_2O_4$

Citation: Chi, Z.; Asher, J.J.; Jennings, M.R.; Chikoidze, E.; Pérez-Tomás, A. Ga_2O_3 and Related Ultra-Wide Bandgap Power Semiconductor Oxides: New Energy Electronics Solutions for CO_2 Emission Mitigation. *Materials* **2022**, *15*, 1164. https://doi.org/10.3390/ma15031164

Academic Editors: John Buckeridge and Ichimura Masaya

Received: 17 December 2021
Accepted: 25 January 2022
Published: 2 February 2022

1. Introduction

According to the latest Intergovernmental Panel on Climate Change (IPCC) report released in August 2021 [1], climate change is widespread, rapid, and intensifying and some trends are now regarded as irreversible. Human-induced climate change is already affecting many weather and climate extremes in every region across the globe. Scientists are also observing changes across the whole Earth's climate system; in the atmosphere, in the oceans, ice floes, and on land. Many of these changes are unprecedented and some of the shifts are now in motion, while some—such as rising sea levels—are already irreversible for the coming centuries to millennia. Stabilizing the climate will require strong, rapid, and sustained reductions in greenhouse gas emissions, and reaching net zero CO_2 emissions. Limiting other greenhouse gases and air pollutants, especially methane, could be beneficial for the health of the climate as well as the population [1]. The breakdown for the different greenhouse gas emissions can be seen in Figure 1 [2], where transport

and electrical production account for up to 40%. Therefore, many energy-related megatrends of our modern society must focus on themes such as energy efficiency, e-mobility, smart grid and digitalization requiring green energy management electronics or power electronic solutions [3].

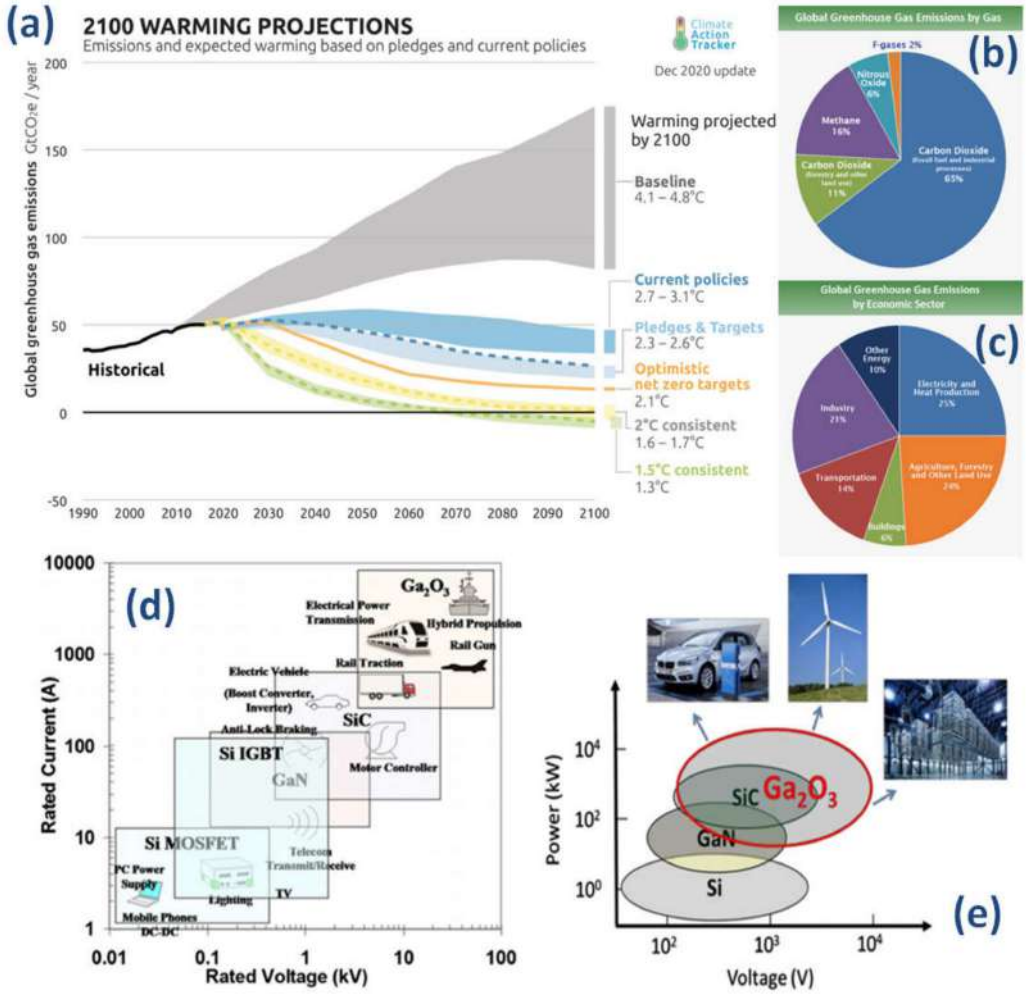

Figure 1. (**a**) Projected global warming figures for 2100. (**b**) Global warming emissions by gas. (**c**) Global greenhouse gas emissions by economic sector. (**d**) Selected applications for power semiconductors Si, SiC, GaN, and Ga_2O_3 for power electronics in terms of current and voltage requirements. (**e**) Owing to its ultra-wide bandgap, Ga_2O_3 can create additional possible applications for ultra-high power electronics including fast chargers for electric vehicles, high voltage direct current (HVDC) for data centers, and alternative energy sources. Figure sources: https://www.epa.gov/ghgemissions/global-greenhouse-gas-emissions-data (accessed on 16 December 2021). Source: (**a**) Source: IPCC (2014); based on global emissions from 2010. Details about the sources included in these estimates can be found in the Contribution of Working Group III to the Fifth Assessment Report of the Intergovernmental Panel on Climate Change. (**b**) IPCC (2014) based on global emissions from 2010. Details about the sources included in these estimates can be found in the Contribution of Working Group III to the Fifth Assessment Report of the Intergovernmental Panel on Climate Change. (**c**) Boden, T.A., Marland, G., and Andres, R.J. (2017). Global, Regional, and National Fossil-Fuel CO_2 Emissions. Carbon Dioxide Information Analysis Center, Oak Ridge National Laboratory, U.S. Department of Energy, Oak Ridge, Tenn., U.S.A. doi 10.3334/CDIAC/00001_V2017. Panels (**d**) and (**e**) adapted with permission from [4](© 2018 COPYRIGHT AIP Publishing).

Around half of the power used in the world is electrical and this is expected to increase steadily in the near future [5]. The vast majority (if not all) of this electricity will flow

through, at least, one power electronic device during its generation, transmission, and final use. This is a critical aspect of power management which is sometimes overlooked, as power electronics make renewable (and non-renewable) energy impactful by increasing their efficiency [6]. As Si-based devices are replaced with other materials which are more energy efficient, this will affect the overall power consumption which will have a knock-on effect on CO_2 emissions by a significant amount [7]. Furthermore, devices made with a semiconductor having a bandgap larger than silicon can be made with less material and have lower cooling requirements, hence saving a lot of space and weight in applications such as electrical transport. This integration obviously impacts the amount of power required and, therefore, saves energy and its associated emissions. Since the 1980s, there has been a lot of work towards replacing silicon-based (E-gap of 1.12 eV) power electronics devices with wide bandgap (3–3.4 eV) semiconductor (WBG) based devices (in particular, silicon carbide (SiC) and gallium nitride (GaN)) and power devices with superior specs (higher temperature of operation, higher power handling capability, etc.) are now commercially available (typically in the range of 650 V–3.5 kV) [8,9] (Figure 1). While SiC devices and GaN transistors are already qualified in many emerging applications, silicon-based devices are still dominating in most applications. There are several reasons for this dominance, to start with, Si-based devices still have substantial potential. Their electrical and thermal performance is outstanding, their reliability is proven as can be seen from their years in application, as well as their low cost. In contrast WBG devices are starting their development, where we are still learning about materials development and device design. The benefits on the system level needs to be qualified and long-term reliability issues need to be determined; as these materials are developed, the costs for high-quality large volume production should decrease.

More recently, the frontier in the field is now given by ultra-wide bandgap semiconductors (UWBG), which have the promise of further upshifting the power rating and operation temperature. The same UWBG oxides also offer the potential for deeper ultraviolet optoelectronics [10]. Although another UWBG semiconductor, diamond, has been investigated over the last forty years, there has been limited progress and only recently have other materials, such as gallium oxide (Ga_2O_3) or aluminum nitride (AlN), yielded device demonstrations with appropriate performances. In particular, Ga_2O_3 is a newer UWBG material (4.5–5 eV) and is receiving a lot of attention as a novel semiconductor, owing to its unusual material properties. The doping (*n*-type) is very tunable with an extremely high breakdown field and unique optoelectronic properties, these alongside the possibility of growing large native substrates (over 6″) with a low cost [11]. Besides, representing the first viable oxide semiconductor for power electronics, Ga_2O_3 has opened the door to many more oxide compounds to be scrutinized (e.g., spinel $ZnGa_2O_4$) as they represent the largest family of ultra-wide bandgap semiconductors. UWBG oxide semiconductors are now at the very frontier of energy electronics, and much cutting-edge research, challenges, and opportunities are taking place [12]. These will be succinctly overviewed in this paper.

2. Oxide Semiconductors for Power Electronics

As an alternative to silicon, there is a new generation of wide bandgap semiconductors which have the capability to operate at higher voltages, temperatures, and switching frequencies with greater efficiencies compared to existing Si devices. This characteristic results in lower losses and enables significantly reduced volume due to decreased cooling requirements and smaller passive components contributing to overall lower system cost. Wide bandgap semiconductors (in the context of power electronic devices) usually represent materials whose band gap is larger than that of silicon. A (non-exhaustive) list of different wide bandgap semiconductors is presented in Figure 2. There are several families of wide bandgap semiconductors depending on their chemical composition. The III–V wide bandgap semiconductors are primarily nitrides, phosphides, and arsenides. Chalcogen semiconductors are those containing a transition metal and a chalcogen anion (S, Se, or Te), therefore forming sulfides, selenides, and tellurides. There are few halogen wide bandgap

semiconductors in the form of chloride, iodides, and bromides. Silicon carbide (which exhibits a very large number of polytypes) and diamond are both carbon-based materials. SiC is a relevant wide bandgap semiconductor since it is the only compound semiconductor that can be thermally oxidized to form SiO_2 in the same fashion as silicon [13].

Group	Material	Formula	Band gap (eV)
III-V			
III-V	Boron nitride, cubic	C-BN	6.36
III-V	Boron nitride, hexagonal	H-BN	5.96
III-V	Aluminium nitride	AlN	6.28
III-V	Aluminium gallium nitride	$Al_xGa_{1-x}N$	3.44-6.28
III-V	Boron arsenide	$B_{12}As_2$	3.47
III-V	Gallium nitride	GaN	3.44
III-V	Indium gallium nitride	$In_xGa_{1-x}N$	2.0-3.44
III-V	Aluminium phosphide	AlP	2.45
Carbon Based			
IV	Diamond	C	5.47
IV	Silicon carbide, 4H-SiC	4H-SiC	3.3
IV	Silicon carbide, 6H-SiC	6H-SiC	3.0
IV	Silicon carbide, 3C-SiC	3C-SiC	2.3
Chalcogens			
II-VI	Calcium sulfide	CaS	5.38
II-VI	Magnesium Sulfide	MgS	4.45
II-VI	Zinc sulfide	H-ZnS	3.91
II-VI	Zinc sulfide	C-ZnS	3.54
II-VI	Magnesium Selenide	MgSe	3.6
II-VI	Magnesium Teluride	MgTe	3.49
II-VI	Maganese teluride	MnTe	3.2
II-VI	Maganese sulfide	MnS	3.1
II-VI	Zinc selenide	ZnSe	2.7
II-VI	Maganese selenide	MnSe	2.65
II-VI	Cadmium sulfide	CdS	2.42
II-VI	Zinc telluride	ZnTe	2.25
$I-III-VI_2$	Cupper Aluminum Sulfide	$CuAlS_2$	3.50
Halogens			
I-VII	Cuprous chloride	CuCl	3.4
I-VII	Cuprous bromide	CuBr	2.91
I-VII	Cuprous iodide	CuI	2.95

Group	Material	Formula	Band gap (eV)
Oxides			
Insulator	Aluminum oxide	Al_2O_3	9.00
Insulator	Magnesium oxide	MgO	7.80
Insulator	Lanthanum aluminate	$LaAlO_3$	5.6
Insulator	lithium metagallate	α-$LiGaO_2$	5.6
Insulator	lithium metagallate	β-$LiGaO_2$	5.6
Semi	Gallium Oxide	α-Ga_2O_3	5.2
Semi	Gallium Oxide	β-Ga_2O_3	4.9
Semi	Magnesium gallate	$MgGa_2O_4$	4.9
Semi	Zinc Germanate	Zn_2GeO_4	4.68
Semi	Zinc Gallate	$ZnGa_2O_4$	4.60
Semi	Indium Germanate	$In_2Ge_2O_7$	4.43
Semi	Silver metagallate	$AgGaO_2$	4.12
Insulator	Lithium niobate	$LiNbO_3$	4
Semi	Zinc Alluminate	$ZnAl_2O_4$	3.8
Semi	Tin dioxide	SnO_2	3.7
Semi	Nickel oxide	NiO	3.6
Semi	Zinc oxide	ZnO	3.37
Semi	Strontium titanate	$SrTiO_3$	3.3
Semi	Titanium dioxide	a-TiO_2	3.2
Semi	Titanium dioxide	r-TiO_2	3.02
Insulator	Barium titanate	$BaTiO_3$	3
Semi	Indium Oxide	In_2O_3	2.9
Semi	p-type delafossite	$CuAlO_2$	3.5
Semi	p-type delafossite	$CuGaO_2$	3.6
Semi	p-type delafossite	$SrCu_2O_2$	3.2

Figure 2. Wide bandgap semiconductors (in the context of power electronic devices) usually representmaterialswhosebandgap is larger than that of silicon. In practice, wide bandgap materials of choice have a bandgap of around ~3 eV, with silicon carbide and gallium nitride in a prominent position. Recently, a new family of semiconductor materials with even larger bandgaps (known as ultra-wide bandgap semiconductors) is being investigated for the new generation of optoelectronic and power electronic applications. As a rule of thumb, an ultra-wide bandgap semiconductor is one whose bandgap is larger than that of GaN (i.e., 3.4 eV). Perhaps the most investigated ultra-wide bandgap semiconductors are diamond, some nitrides (AlGaN, AlN, and BN), and a few oxides. Among these oxides, gallium oxide is the only oxide semiconductor with ultra-large bandgap where it is possible to modulate the conductivity (i.e., doping) to define power electronic devices.

A special case of chalcogenides would be oxides; although group 16 is defined as chalcogens, the term chalcogenide is more commonly reserved for sulfides, selenides, and tellurides only. Oxides are ubiquitous in nature due to the large abundance of oxygen in the earth and the large oxygen electronegativity (i.e., the atom tendency to attract electrons and thus form bonds) that easily creates largely covalent stable chemical bonds with almost all elements to give the corresponding oxides. Indeed, almost the entire Earth's crust parts are oxides as the individual crust elements are inclemently oxidized by the oxygen present in the atmosphere or in the water [14]. Besides, the Earth's mantle (which represents 60–70% and ~80% of the Earth's mass and volume, respectively) is predominantly a layer of silicate (i.e., compounds containing silicon and oxygen including silica, orthosilicates, metasilicates, pyrosilicates, etc.) and magnesium oxide (MgO)-rich rock between the crust

and the outer core [14]. The upper mantle is dominantly peridotite, composed primarily of variable proportions of the minerals olivine ($(Mg,Fe)_2SiO_4$), pyroxenes ($XY(Si,Al)_2O_6$), and aluminous phases, such as feldspar ($NaAlSi_3O_8$–$CaAl_2Si_2O_8$) and spinel ($MgAl_2O_4$). The lower mantle is composed primarily of bridgmanite ($(Mg, Fe)SiO_3$) and ferropericlase ((Mg, Fe)O), with significant amounts of calcium perovskite ($CaSiO_3$) and calcium-ferrite oxides [15].

Thus, in general, oxides can be regarded as naturally abundant and stable compounds. Since the early days of solid-state physics, (undoped) oxides have been considered to be insulators (or more precisely, highly resistive wide bandgap semiconductors). The bandgap of many common oxides, such as Al_2O_3, SnO_2, TiO_2, In_2O_3, Cu_2O, WO_3, ZnO, or NiO, is much wider than that of silicon (1.12 eV). Therefore, they are intrinsically poor conductors at room temperature if they are not properly doped into a degenerated state. Recently, much effort has been put into increasing the conductivity of some of these oxides (in particular those where *s* and *p* electrons propagate with a large mobility) while maintaining the optical transparency. Good examples are the doping of Al in ZnO, Sn in In_2O_3, and F in SnO_2, which are known as transparent conducting oxides (TCOs).

In practice, wide bandgap materials of choice have a bandgap of around ~3 eV, with silicon carbide and gallium nitride in a prominent position. Recently, a new family of semiconductor materials with even larger bandgaps (known as ultra-wide bandgap semiconductors) is being investigated for the new generation of optoelectronic and power electronic applications. As a rule of thumb, an ultra-wide bandgap semiconductor is one with a band gap larger than that of GaN (i.e., 3.4 eV). Perhaps the most investigated ultra-wide bandgap semiconductors are diamond, some nitrides (AlGaN, AlN, and BN), and few oxides. Among oxides, gallium oxide (Ga_2O_3) is the only oxide semiconductor with ultra-large bandgap where it is possible to modulate the conductivity (i.e., doping) to define power electronic devices. SiC and GaN power devices have already attracted much attention in higher efficiency electrical power conversion [4]. The major advantage of β-Ga_2O_3 is that the single crystal structure can be synthesized via several standard melt growth methods, e.g., the Czochralski (CZ) technique. This is a huge advantage of Ga_2O_3 over SiC, GaN, and diamond for scaling up production, hence we would expect the cost of β-Ga_2O_3 power electronics to decrease and be more in line with silicon with respect to their SiC and GaN counterparts [16,17].

3. Gallium Oxide (Ga_2O_3)

Ga_2O_3 has, at least, six polymorphs of which only one is thermodynamically stable at high temperatures (β phase, monoclinic), while the others are metastable and tend to convert to β upon high-temperature treatments including the phases α, corundum, δ, cubic, and ε, hexagonal, γ, defective-spinel, and orthorhombic κ polymorph [18]. The basic principles of polymorphism in crystals are clear: the lattices adapt to the minimum energy with respect to the temperature and pressure. Nearly all Ga_2O_3-containing devices utilize the monoclinic β phase, the most stable and best-characterized polymorph. As a well-known representative of a binary metal-oxide, gallium oxide cannot therefore be regarded as a new material, but as a revisited and rejuvenated one. For example, early crystallographic studies for single crystals [19] together with diverse luminescence studies of doped β-Ga_2O_3 were reported as early as the1960s [20]. Lorenz et al. [21] already published in 1966 that *n*-type Ga_2O_3 exhibits mobilities in the range of 100 $cm^2V^{-1}s^{-1}$ and an adequate device doping of 10^{18} cm^{-3} can be achieved just by controlling the native oxygen vacancies' density. Its deep-ultraviolet intrinsic bandgap of around 4.5–4.9 eV and excellent photoconductivity are also well-known from early contemporary studies [22]. It was not until this decade that the potential of Ga_2O_3 for a certain class of extreme or power electronics was realized due to further availability of large-area single crystals with high quality and the control of doping. In the past, Ga_2O_3 was somehow ignored as an ultra-wide bandgap material, as it was eclipsed by the potential of diamond which has never been fully realized [23].

Previously, SiC and GaN were the wide bandgap materials of choice [6]. However, from an ultra-high energy electronics perspective, Ga_2O_3 transistors and diodes exhibit the potential of delivering outstanding performances in the form of high breakdown voltage, high power and low losses because of superior material properties, thus extending the power handling limits given by the SiC and GaN integration into the mainstream [4]. Indeed, an ultra-large breakdown electric field, (which is usually assumed to be of the order of E_c~8 MVcm^{-1}), is a prime material advantage of Ga_2O_3. However, this value may be well underestimated; it was very recently suggested that the critical electric field of Ga_2O_3 could be as large as 13.2 MVcm^{-1}, if the residual donors are efficiently removed [24].

A high critical field crucially promotes the suitability of a semiconductor material for power devices that would be able to manage a large amount of electrical energy per unit area. Baliga's figure of merit [25] for power electronics is proportional to E_c^3, whilst only being linearly proportional to the bulk electron mobility (μ). Although Ga_2O_3 presents a similar conduction band dispersion (i.e., effective mass) than GaN, a relatively small bound limit of μ ~300 cm^{2}V^{-1}s^{-1} is frequently given [26]. This is due to a massive Fröhlich interaction which is common to many conducting oxides. Balancing critical field and mobility, the on-state losses can be still an order of magnitude lower than those for SiC and GaN for a given breakdown voltage (Figure 3). Comparing these values to other power semiconductors (see Figure 3), β-Ga_2O_3 appears favorable, surpassing SiC and GaN. A major additional technological advantage of the β-Ga_2O_3 is that the single crystal structure can be synthesized via several standard melt growth methods including the Czochralski (CZ) technique [27]. This, in practice, would imply SiC performances (or better ones) at a fraction of cost.

WBG	Bandgap E_g [eV]	Permitt. ε_r [ε_0]	Mobility μ_n [cm^2/Vs]	Crit. Field E_c [MV/cm]	BFOM x10^6 [V^2/Wcm^2]	Ther. Cond. k [W/mK]
Si	1.12	11.9	1240	0.3	8.8	145
4H-SiC	3.20	9.7	980	3.1	6270	350
GaN	3.40	10.4	1000	4.9	27900	140
β-Ga_2O_3	4.90	10.0	150	10.3	36300	27
Diamond	5.50	5.7	2000	13.0	554000	3450
AlN	6.00	9.8	426	15.4	336000	319
c-BN	6.40	7.1	825	17.5	695000	2145

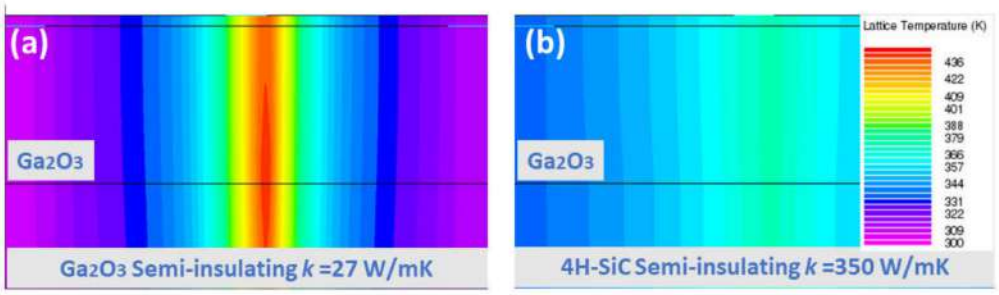

Figure 3. A summary of the main power device figure of merit (or Baliga's figure of merit. BFOM) parameters of the most popular wide bandgap semiconductors. Gallium oxide has a particularly poor thermal conductivity. However, when integrated into devices, heterojunctions with other better suited heat sinks (such as silicon carbide) area way to circumvent that limitation. As shown in the bottom panels, the simulate lattice temperature is lower on SiC (**b**) when compared with Ga_2O_3 substrates (**a**). Furthermore, thinning the Ga_2O_3 active film helps thermal performances. Adapted with permission from [11] © 2018 COPYRIGHT Society of Photo-Optical Instrumentation Engineers (SPIE).

There are certain applications, such as maritime and air transport, that are difficult to electrify as the power ratings are generally larger than, say, urban electric cars (Figure 1d,e).

For electric cars, devices delivering at or below the 1.2 kV perform well as rapid chargers or drive converters. These power ratings are well covered with "conventional" WBG, such as SiC and GaN. As the critical electric field of Ga_2O_3 has been reported to be at least two times, (or even four times larger), than that of these WBGs, the blocking voltage range of single electronics devices may be significantly extended in the future beyond what is theoretically possible today. These promises will impact directly on the size and weight of planes and ships resulting in less energy and emissions. As energy and transportation represents a major portion of the current CO_2 emissions contributing to global warming, it is expected that UWBG such as Ga_2O_3 may open new opportunities in sectors that are now difficult to decarbonize. Other prominent examples where the advantage of ultra-wide bandgap semiconductors can be exploited are as more solar-blind (UV transparent) transparent conducting electrodes [11] and electron (or hole) transport layers within solar cells or photodiodes [28].

3.1. Gallium Oxide Bulk Crystal Growth

Commonly used growth techniques of bulk β-Ga_2O_3 crystal are (Table 1): Verneuil method [21,29], Czochralski (CZ) method [30–33], floating-zone (FZ) method [34], edge-defined film fed (EFG) method [16,17], and Bridgman (horizontal or vertical, HB and VB) method [35,36],summarizing the basic features of melt growth methods reported so far.

Table 1. Overview of β-Ga_2O_3 bulk crystal growth methods.

Method	Verneuil	FZ	CZ	EFG	VB
Schematic illustration	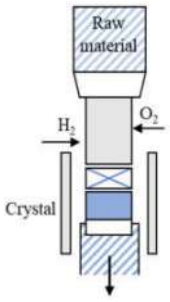	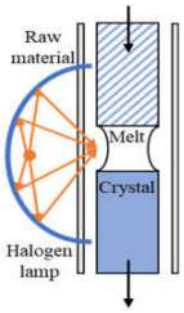	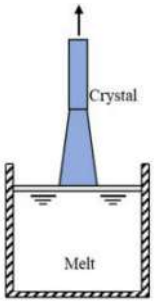	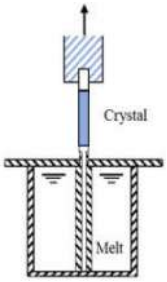	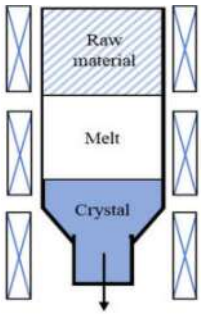
Bulk size	3/8-inch diameter 1-inch length	1-inch diameter	2-inch diameter	6-inch width 4-inch diameter	2-inch diameter
Growth rate (mm/h)	10	20–40	2	15	5
FWMH	-	22 arcsec	22–50 arcsec	17 arcsec	10–50 arcsec
Dislocation density	-	-	~10^3 cm^{-2}	10^3 cm^{-2}	10^2–2 ×10^3 cm^{-2}
Residual impurity	2 × 10^{18}cm^{-3}	~10^{17} cm^{-3} (Si, Sn)	~10^{16} cm^{-3} (Si)	~10^{17} cm^{-3} (Si)	~several tens wt.ppm (Rh)
Intentional doping	~10^{19} cm^{-3} (Mg), ~10^{21} cm^{-3} (Zr) at 900 °C	~10^{19} cm^{-3} (Nb, Ta)	~10^{19} cm^{-3} (Sn, Si, Hf)	6-7 × 10^{18} cm^{-3} (Si, Sn)	3.6 × 10^{18} cm^{-3} (Sn)
Refs.	[21,28,37,38]	[34,38–43]	[16,17,30,33,43–45]	[16,17,46,47]	[35,36,48]

The Verneuil method, being a crucible-free technique, enables both oxidizing and reducing of growth conditions [21]. The synthesis under a reducing condition benefited electron conductivity [49]. *N*-type doping was realized by Harwig et al. [37], the free carrier concentration was determined to be ~10^{19} cm^{-3} by Mg doping, and ~10^{21} cm^{-3} by Zr doping at 900 °C. The β-Ga_2O_3 bulk crystal grown by this method has poor quality, and it was used mainly last century, as other more efficient techniques were well developed. The FZ method is also a crucible-free technique, it was recently used to grow bulk β-Ga_2O_3 crystal to investigate the scintillation features [50,51] as it can be employed in an air atmosphere, which may allow for creation of fewer oxygen defect centers being the emission origin of Ga_2O_3 [52]. Tomioka et al. [41] analyzed the residual impurities of β-Ga_2O_3 grown by the FZ method by inductively-coupled plasma mass spectroscopy; besides Si or Sn, Al, Mg, and Fe have also been detected with a concentration of ~10^{16} cm^{-3}. Al was presumed to be a neutral impurity, while Mg and Fe were considered as deep ionized acceptors and could compensate Si donors. To our knowledge, the lowest FWHM reported is ~22 arcsec

for the peak β-Ga_2O_3 (400) by Hossain et al. [39], in this work, the Laue diffraction patterns also confirmed that the grown β-Ga_2O_3 crystal has a good crystallinity. However, FWHM of β-Ga_2O_3 rocking curves larger than 100 arcsec has also been measured [38,53]. However, both these techniques mentioned above suffer from small crystal size (wafer is no more than 1 inch so far, as summarized in Table 1.

Using an Ircrucible, the CZ method has been predicted to be a potential candidate for large boule, but thermal instability is an issue at high temperature that leads to decomposition of Ga_2O_3. Thus, this technique requires atmosphere control. Being a crack-free technique, the β-Ga_2O_3 crystal grown by the CZ method has small or even no boundaries. Several works reported by Galazka et al. [32,43,44] evidenced that the FWHM of the X-ray rocking curve could be as low as 22–50 arcsec on average, and the dislocation density was ~103 cm^{-2}. Moreover, Galazka et al. [31] recently reported that bulk Ga_2O_3 grown by the CZ method has an electron mobility of 80–152 $cm^2V^{-1}s^{-1}$ with a low residual Si impurity concentration of ~10^{16} cm^{-3}. Similar to the CZ method, the EFG method has the same technique issue. However, this technique is available for a 4-inch wafer and recently became commercially available. Commonly observed twin-boundaries in the EFG grown β-Ga_2O_3 were efficiently avoided by optimizing the growth process (the so-called shouldering process). Different from the traditional growth direction (010), Oshima et al. [54] demonstrated that the (001) oriented β-Ga_2O_3 grown by the EFG is more suitable than (010) for a Schottky barrier diode (SBD). A weak correlation between pits and electrical properties has been revealed [27,54]. The use of the VB method allows withstanding of high oxygen concentrations as a Pt-Rh (70–30%) alloy crucible. Additionally, this crucible also facilitates the pulling-up process as the grown crystal does not adhere to the wall. The major residual impurities are generally Rh (~several tens wt.ppm) from the crucible, Sn and Si (~several wt.ppm) from raw materials, and Fe and Zr (~several wt.ppm) from the furnace [36,48].This technique recently became *n*-type doping available by using a resistance heating VB furnace, and electron concentration and electron mobility were determined to be 3.6 × 10^{18} cm^{-3} and 60 $cm^2V^{-1}s^{-1}$, respectively, by 0.1 mol% Sn-doped [35,48]. As the CZ, EFG, and VB method use the crucible, they all have a high level of scalability.

3.2. Gallium Oxide Thin-Film Growth

Bulk devices and subsequent epitaxy of β-Ga_2O_3 layers could be provided by bulk growth, while high-quality epitaxial growth technologies are still required in order to study and fabricate more complex devices. Halide vapor phase epitaxy (HVPE), metal-organic vapor phase epitaxy (MOVPE), pulsed laser deposition (PLD), atomic layer deposition (ALD), molecular beam epitaxy (MBE), mist-chemical vapor deposition (CVD), and metal-organic chemical vapor deposition (MOCVD) are all involved in thin-film growth of Ga_2O_3.

Vapor phase epitaxy is a commercially promising technique for mass production of β-Ga_2O_3. Based on VPE, the halide vapor phase epitaxy (HVPE) method enables a growth rate as high as 250 μm/h [55] and the wafer size from 2 to 6 inches [56], it is thus a suitable technique for thick films with high purity for high voltage vertical switching devices. Furthermore, with the presence of chlorine catalyst in the growth chamber, this technique exhibits the growth of metastable phases of Ga_2O_3, such as α and ε [57]. The HVPE method suffers from a high level of roughness on the surface even at a relatively low growth rate [56,58]; an electrical mechanical [59] or a chemical mechanical [60] polishing can be employed to remove further deep surface pits formed during the growth. Leach et al. [61] reported a vast difference in surface morphology and XRD full-width half-maximum (FWMH), between sufficiently and insufficiently CMP polished (discriminated by the polishing times of the various polishing steps) β-Ga_2O_3 wafers grown by HVPE. Despite the poor morphology, the FWHM of the films grown on on-axis substrate were as narrow as 28 arcsec. Moreover, Murakami et al. [62] revealed that effective donor concentration without intentional doping could reach as low as 10^{13} cm^{-3}.

Metal-organic vapor phase epitaxy (MOVPE)can provide a highly scalable growth as its deposition areas are large. Triethylgallium (TEGa), trimethylgallium (TMGa), and $O_2$are

most commonly the precursors for gallium and oxygen, respectively. The homoepitaxial growth of β-Ga_2O_3 by MOVPE can be strongly affected by substrate orientation. The growth rate is approximately 1.6–2.0 nm/min on the (100) plane, 0.65–1 µm/h on the (010) plane, and 1.6–4.3 nm/min on the (00-1) plane with miscut angles [63]. Recently, the growth rate can be elevated to 3.6 nm/min on the (100) plane [64] by tuning the growth pressure. A high-quality homoepitaxial growth on β-Ga_2O_3 the (100) with an FWMH of 43 arcsec has been reported by Gogova et al. [65]. The study of residual donor source is still in progress [66] while an electron concentration of 8×10^{19} cm^{-3} by Si-doping was realized by Baldini et al. [67], which is the highest doping level by this technique so far.

Pulsed laser deposition (PLD) has often been used for doped layers of Ga_2O_3 as it can transport materials from the target to the substrate stoichiometrically, thus the thickness of layers can be incisively controlled. It also has a relatively low operating temperature compared to other techniques. However, the quality of the materials deposited and the deposition rate are relatively low compared with other CVD and MBE methods. The roughness measured on the surface of Ga_2O_3 films had a root mean square between 1 and 7 nm [68–70].

A growth rate of 10.8 nm/min could be reached without oxygen, while it decreased to 6.5 nm/min by increasing oxygen pressure to 50 mbar [71]. Indeed, oxygen partial pressure and temperature are considered as the dominant parameters for properties of materials grown by the PLD [72]. The crystallinity was enhanced by increasing oxygen pressure at either low deposition temperature (250 °C [71]) or high deposition temperature (780 °C [68]). A higher oxygen partial pressure also leads to self-trapped holes at O1*s* and between two O2*s* sites [68], which could further act on the transport properties. Unlike the influence of oxygen pressure, a higher temperature does not always lead to a better film quality [73,74]. While, as expected, a higher annealing temperature could improve the crystallinity, as it helps the re-arrangement of Ga and O atoms to their optimal sites [75,76]. The highest *n*-type doping level achieved by the PLD is 1.7×10^{20} cm^{-3} by Si doping [69].

Atomic layer deposition (ALD), initially called atomic layer epitaxy (ALE), is a sub-set of the chemical vapor deposition (CVD) technique based on self-saturation, sequential surface reactions. ALD is a more general deposition containing ALE and molecular layering (ML) techniques [77]. The highly controlled thickness of films and conformal coverage are the main advantages of ALD over other techniques, it also allows a relatively lower deposition temperature compared to MBE and CVD techniques and a lower growth rate (generally less than 0.1 nm/cycle). Sn-doped Ga_2O_3 grown by ALD was investigated by Siah et al. [78], however the concentration of Sn was estimated as 2×10^{20} cm^{-3}, with the free electrons determined to be 4×10^{18} cm^{-3}. This was due to the low growth temperature.

Thus, post-annealing is generally also required to improve the crystalline quality. Additionally, the temperature during growth depends mainly on the gallium precursor chosen [79,80]. Besides the conventional ALD, the plasma-enhanced atomic layer deposition (PEALD) further permits a lower deposition temperature and better Ga_2O_3film properties with very smooth surface roughness (<1 nm) [81–83].

Molecular beam epitaxy (MBE)suits research purposes better than commercial use, as it enables the growth of high structural quality β-Ga_2O_3 with a relatively low growth rate (<1 µm/h) and high production cost, while high voltage vertical devices often require thick drift regions (dozens of microns). The orientation of growth has been found to be one factor that influences the growth rate [84]. Mazzolini et al. [85] further demonstrated the growth rate of different orientations Γ(010) (2.3 nm/min) > Γ(001) > Γ(−201) > Γ(100) of In-catalyzed β-Ga_2O_3layers;this phenomenon was believed to be associated with the surface free energy related to the binding energy of the In ad-atom. Nepal et al. [86] reported a heteroepitaxial growth on SiC with (−402) having a relatively high FWMH (694 arcsec), which can be reduced to 30–60 arcsec by homoepitaxial growth [87]. The thin films grown by MBE also benefit a smooth surface with a roughness of less than 1 nm [88,89]. The densities of the threading dislocation etch pits was determined to be ~10^5 cm^{-2} for the film grown at 850 °C [89]. An electron concentration of 10^{20} cm^{-3} has been achieved by Sn doping [90].

Techniques based on chemical vapor deposition (CVD) have also been employed for the growth of Ga_2O_3. Scalability and mass production are the most advantageous characteristics of the mist-CVD technique, as it is a vacuum free, low-cost, and solution-processed approach. This technique is also often used for epitaxial growth of α-Ga_2O_3 on sapphire [91–94]. Morimoto et al. [94] also pointed out the facilities of mist-CVD for $Ga_2O_3$by F doping. Both homoepitaxial [95,96] and heteroepitaxial [97] growth of β-Ga_2O_3have been successfully performed. It is also worth noting that the FWMH of rocking curves was 39–91 arcsec for homoepitaxial growth with growth rate of 0.5–3.2 µm/h [96,98]. An electron concentration was measured as 5×10^{20} cm^{-3} by Sn doping [98].

The metal-organic chemical vapor deposition (MOCVD) technique uses Ga-based organic material as metal precursors, such as trimethylgallium (TMGa) and triethylgallium (TEGa), which usually leads to C-contamination of the as-grown film (relatively less carbon by using TEGa than TMGa). It is well-known that such contamination can be efficiently reduced by high growth temperature, and eliminated by post-annealing. Li et al. [99] reported a high-quality homoepitaxially grown film with FWMH and surface roughness of 21.6 arcsec and 0.68 nm, respectively. The growth rate is generally from several hundred nm/h [100,101] to10 µm/h [102–104]. This technique is also available for both *n*- and *p*-type dupability [24,105] (Figure 4).

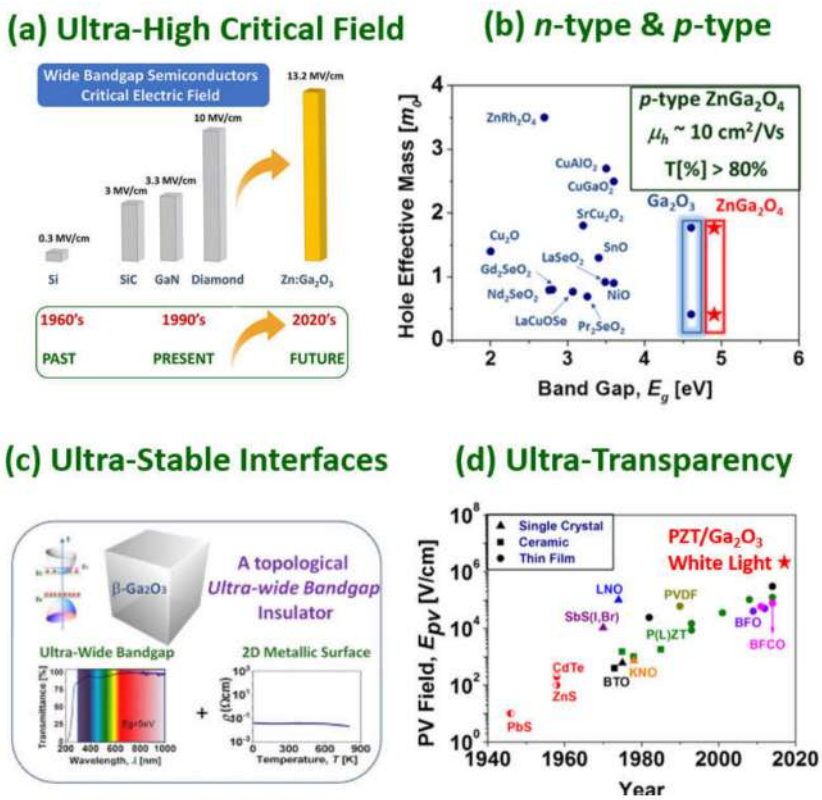

Figure 4. Ga_2O_3 and related oxides have been demonstrated to exhibit some remarkable features, such as (**a**) ultra-high critical electric field, (**b**) potential bipolar operation due to its demonstrated *n*-type and *p*-type conductivity, (**c**) ultra-stable interfaces that may host a 2D electron gas, (**d**) extended transparency into the UV-A region for transparent conducting oxide (TCO) applications (tail state density is located deeper in the ultraviolet than conventional TCOs). Panel (**a**) adapted with permission from Chikoidze et al. [24] © 2022 Elsevier Ltd. All rights reserved. Panel (**b**) adapted with permission from Chikoidze et al. [106] Copyright © 2022, American Chemical Society. Panel (**c**) adapted with permission from Chikoidze et al. [107]. © 2022 Elsevier Ltd. All rights reserved. Panel (**d**) adapted with permission from Perez-Tomas et al. [108,109] © 2022 WILEY-VCH Verlag GmbH & Co. KGaA. Adapted with permission from [12] © 2021 COPYRIGHT Society of Photo-Optical Instrumentation Engineers (SPIE).

3.3. Gallium Oxide Doping Issues and Recent Progress

β-Ga_2O_3 is very easily doped *n*-type to the degenerate state, *n*-type doped β-Ga_2O_3 with carrier concentration from 10^{16} to 10^{20} cm^{-3} [110,111] has been achieved by Sn and Ge doping by MBE, Si and Sn doping by MOVPE, and Sn doping by MOCVD [69]. A high mobility at room temperature of 145–184 $cm^2V^{-1}s^{-1}$ [100,101,112] has been reached by Si doping, and even till 10^4 $cm^2V^{-1}s^{-1}$ at 46 K [109]. Having a high critical field (5.2 $MV.cm^{-1}$ without intentional doping [113]), the β-Ga_2O_3devices demonstrate high performance. Nevertheless, all the Ga_2O_3devices demonstrated thus far have been unipolar in nature (i.e., only *n*-type). In order to realize the full potential for WBG opto-electronics β-$Ga_2O_3$and to sustain high breakdown voltage (>6.5 kV), we need vertical geometry bipolar-junction-based devices. Therefore, the realization of *p*-type β-Ga_2O_3 is a primary challenge today for the gallium oxide scientific community (Figure 4).

There is a tendency in oxide compounds to have *n*-type conductivity, caused by vacancies in the oxygen atoms. This, as well as the fact that it is a UWBG material, intrinsic conduction is rare and even causes *p*- and *n*-type doping tends not to be symmetrical. This asymmetry is seen in gallium oxide, the hole conductivity is poor and is likely the main limitation for development of gallium oxide technology. Fundamental restrictions such as this area recurring issue in oxides, such as: (i) acceptor point defects with high formation energy; (ii) native donor defects with low energy—resting holes; and (iii) *p*-type oxides suffer from a high effective mass of the holes (this results in a low mobility), due to the top of the VB predominantly from localized O 2-p derived orbits.

Native *p*-type conductivity: Using thermodynamical calculations for the point defects on gallium oxide it can be seen that gallium oxide is "lucky", as when β-$Ga_2O_3$is at 500 °C, $P_{hole} \approx 1.33 \times 10^{-2}$ atm with a hole concentration around $p \approx 10^{15}$ cm^{-3} [114]. Comparing this to calculations for ZnO gives $P_{hole} \approx 10^3$ atm, for the same temperature. This divergence is believed to be from higher formation energy of the donor vacancies in β-Ga_2O_3 (approximately 1 eV higher per vacancy), making compensation mechanism by point defects less favorable in gallium oxide than in ZnO. As a consequence, it can be expected that *p*-type samples of β-Ga_2O_3 with higher carrier concentrations (then intrinsic) can be obtained when doping with shallow acceptor impurities.

The native hole concentration was investigated by Nanovation (SME, France) [114] where undoped β-Ga_2O_3thin film grown on c-sapphire substrates by pulsed laser deposition (PLD) showing resistivity of $\rho = 1.8 \times 10^2$ Ω.cm, hole concentration of $p = 2 \times 10^{13}$ cm^{-3} and a hole mobility of 4.2 $cm^2V^{-1}s^{-1}$ [114]. The determination of conductivity mechanism showed that Ga vacancies act as deep level acceptors with the activation energy of 0.56 eV in the low compensated sample, having *Ea* = 1.2 eV ionization energy. Later, the improvement was shown that native *p*-type conductivity by post-annealing in an oxygen atmosphere for β-Ga_2O_3 thin film was grown on c-sapphire substrates by MOCVD [115]. After oxygen annealing, the hole concentration was increased from 5.6×10^{14} cm^{-3} to 5.6×10^{17} cm^{-3} at 850 K. The author claimed that the annealing effect is related to the formation of $V_{Ga}{}^{—}V_O{}^{++}$ complexes as a shallow acceptor center with E_a = 0.17 eV activation energy.

Device applications require higher hole concentrations (at operating temperature), which could be achieved via external acceptor impurity incorporation.

There are already extensive theoretical studies (standard density functional theory (DFT and DFT with GGA+U) of acceptor impurity doping of β-Ga_2O_3 in order to identify efficient *p*-type dopant. Kyrtsos et al. [116] demonstrated by DFT calculations that dopants, such as Zn, Li, and Mg, will introduce deep acceptor level with ionization energies of more than 1 eV, thus, they cannot contribute to the *p*-type conductivity. However, this result could be influenced by the underestimation of the bandgap due to the semi-local approach. Varley et al. [117] predicted that self-trapped holes are more favorable than delocalized holes due to their energies and by theoretical calculation (self-trapping energy is 0.53 eV and barrier to trapping is 0.10 eV). This indicates that free holes are unstable and will spontaneously localize towards small polarons.

Lyons [118] examined the elements of group 5 and group 12 (Be, Mg, Ca, Sr, Zn, Cd) as acceptor impurities in β-Ga_2O_3 by hybrid DFT, all of them will exhibit the acceptor ionization levels of more than 1.3 eV. Mg was determined to be the most stable acceptor species, followed by Be. Sun et al. [119] used ab initio calculations to simulate the doping by Ge, Sn, Si, N, and Cl. Among them, N has been predicted to be a deep acceptor with an impurity level of 1.45 eV, as it has a similar atomic size as oxygen but has one less valence electron, and a higher *2p* orbital than oxygen. While all others act as donors, another ab initio calculation also demonstrated that nitrogen doping could introduce an acceptor level at 1.33 eV above the VBM.

Very recently, Goyal et al. [120] simulated a growth-annealing-quench sequence for hydrogen-assisted Mg doping in Ga_2O_3 by using the first principles defect theory and defect equilibrium calculations. The H_2O partial pressure and H exposure can strongly influence the Mg dopants concentration during the growth, by increasing the solubility limit of the acceptor, or by reducing the compensation. A conversion from *n*-type to *p*-type was achieved by annealing at O-rich/H-poor conditions. A Fermi level at +1.5 eV above the VB has been found after quenching.

Doping with two elements (co-doping) has been predicted by DFT which showed a promising method to obtain *p*-type β-Ga_2O_3, as it can break the solubility limit of mono-doping and improves the photoelectric properties of semiconductor materials which results in increasing the conductivity.

The principle is to increase carrier concentration and decrease the compensating defect formation energy. This is inherently caused by the localized nature of the O2 *p*-derived VB that leads to difficulty in introducing shallow acceptors and large hole effective mass [121].

Co-doping has been successfully used for II-VI compounds, co-doping containing N (Zn-N, N-P, Al-N, and In-N) has been demonstrated to be an effective way to improve the *p*-type conductivity [122–124], in particular, Zhang et al. [124] predicted two shallow impurity levels above the VB of about 0.149 eV and 0.483 eV in N–Zn co-doped β-Ga_2O_3. Co-doping by N-P made an acceptor level decrease ~0.8 eV, and an impurity level appears at 0.55 eV above the VB of β-Ga_2O_3. A significant loss of holes' effective mass was also evidenced [124]. There are a few experimental works reported regarding *p*-type doping of gallium oxide. Mg-doped β-$Ga_2O_3$was studied by Qian et al. [125] for the photo-blind detector, and the β-Ga_2O_3 containing 4.92 at% Mg has shown an acceptor level by XPS. A variation of bandgap has also been reported [83,126] however, the Hall effect measurement validity failed at room temperature due to the very high resistivity of the samples [127].

Suet al. [128] deposited Mg-Zn co-doped β-Ga_2O_3 on sapphire (0001), however, anti-sites' impurity defects (i.e., ZnGa and GaZn) were determined as deep acceptors (0.79 eV for ZnGa and 1.00 eV for GaZn) by absorption spectra. Feng et al. [129] demonstrated Zn doping (1.3–3.6 at%) in β-Ga_2O_3nanowires can reduce the bandgap slightly, they also proved the *p*-type conductivity by making *p*-*n* junction. Chikoidze et al. [24] suggested that Zn in β-Ga_2O_3 has an amphoteric nature: it can be an acceptor as Zn_{Ga} defect and at the same time, a donor being in Zn_i interstitial sites. It was shown that in (0.5%) Zn:Ga_2O_3 the auto-compensation of donor (Zn_i) -acceptor (Zn_{Ga}) defects takes place.

Islam et al. [130] reported that hydrogen annealing could vastly reduce the resistivity and reach a remarkable hole density of ~ 10^{15} cm^{-3} at room temperature. Besides, the ionization energy of acceptor is as low as 42 meV by incorporation of hydrogen in the lattice. This improvement is related to hydrogen decorated gallium vacancies $V_{Ga\text{-}H}$: during the diffusion of hydrogen into the Ga_2O_3crystal, H^+ absorbed at the surface will be attracted toward the $V_{Ga}{}^{3-}$, it stabilizes the negative charge and thus lowers the acceptor level. This mechanism leads to H^+ decorated Ga-vacancy $V_{Ga\text{-}2H}{}^{1-}$ and, therefore, the *p*-type conductivity.

Nitrogen-doped *p*-Ga_2O_3 has been experimentally achieved by non-conventional growth technique. Wu et al. [131] demonstrated a multi-step structural phase transition growth from hexagonal $P6_3mc$ GaN to rhombohedral R3C α-$GaN_xO_{3(1-x)/2}$ and realized the monolithic C2/m N-doped β-Ga_2O_3 thin layer finally with an acceptor ionization

energy of 0.165 eV. The resistivity, hole concentration, and hole mobility are 17.0 Ω.cm, $1.56 \times 10^{16} cm^{-3}$, and 23.6 $cm^2V^{-1}s^{-1}$, respectively, by employing the Hall effect measurement. A performant field-effect transistor was also fabricated based on this *p*-type *β*-Ga_2O_3. Clearly, further experimental studies of optimal acceptor defects with room temperature activation are required.

3.4. Gallium Oxide Power Rectifiers

Once the device-grade epitaxial layers have been grown either homo- (bulk Ga_2O_3) hetero- (e.g., sapphire, silicon), or both, the simplest electronic devices one can define are rectifiers. In a Schottky rectifier, the counter-electrode (cathode) is processed to allow low resistance Ohmic contact while the anode contact is intended as a Schottky junction over a lightly doped epitaxy; it conducts electrons in the forward mode while sustaining large electric fields (by the creation of a depletion space charge region) in the reverse mode. As mentioned previously, devices using Ga_2O_3 are primarily limited to unipolar devices and Schottky diodes are made, in general, on *n*-type semiconductor layers as electrons are lighter than holes. However, it is also important to consider the appropriate metal contacts to Ga_2O_3 as they are responsible for connecting the semiconductor to the surrounding electrical circuit/system and parameters such as the Schottky barrier height are crucial. For different contacts to Ga_2O_3, such as in GaN and AlGaN, which utilize stacks of different metals [132], this decision can make an important difference to the nature of the contact. Regarding Schottky contacts to Ga_2O_3,Ni/Au is a common choice (see Table 2). Other Schottky contacts investigated include Pt, Ni, Cu, W, Ir, TiN/Au, Pt/Ti/Au, Ni/Au, ndPt/Au [133–136]. Very recently, an ultra-large Schottky barrier of ~1.8 eV was extracted for all-oxide $PdCoO_2$/*β*-Ga_2O_3 Schottky diodes [137]. The polar layered structure of $PdCoO_2$ generates electric dipoles, realizing a large Schottky barrier height of ~1.8 eV (well beyond the 0.7 eV expected from the basal Schottky–Mott relation) along with a large on/off ratio approaching 10^8, even at a high temperature of 350 °C (Figure 5c). As there are a number of polar oxides, this is a promising approach to increase the reverse blocking voltage of Ga_2O_3 diodes [138].

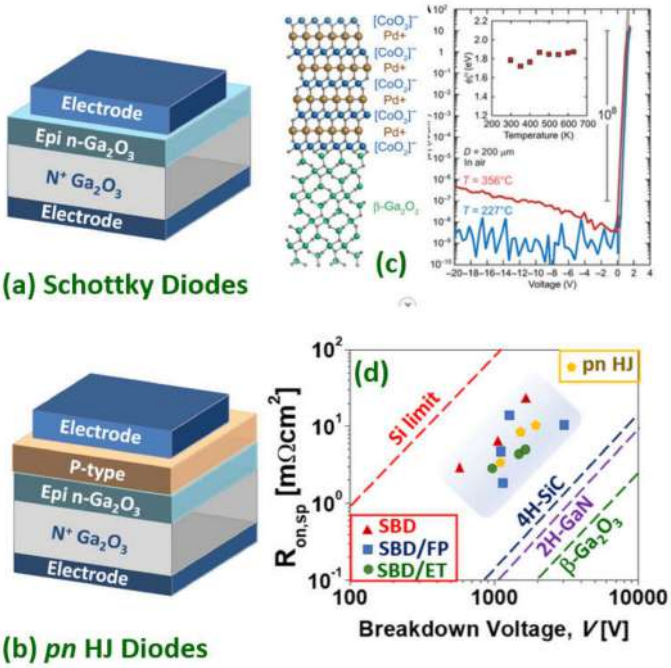

Figure 5. Schematics of (**a**) vertical Ga_2O_3 Schottky diodes and (**b**) *p*-*n* heterojunction diodes. (**c**) A $PdCoC_2/Ga_2O_3$ exhibiting the ultra-large Schottky barrier of 1.8 eV. (**d**) Baliga's FOM for selected Schottky and p-n HJ diodes from the literature. Panel (**c**) adapted with permission from Harada et al. [137] © 2022 AAAS 4.0 (CC BY-NC). Adapted with permission from [12] © 2021 copyright Society of Photo-Optical Instrumentation Engineers (SPIE).

Table 2. Table displaying varying SBD designs: L—lateral, V—vertical, TCO—thin conductive oxide film, FP—field plate, BET—bevel edge termination, FPET—field plate edge termination, MDS—metal-dielectric-semiconductor Schottky diode. Included here are different structures which exhibited SBD (some exhibiting Schottky contacts as opposed to useable device) using a range of different designs and metal stacks.

Device Configuration	Schottky Metal Stack	Ohmic Metal Stack	V_{br}	Ideality Factor	Ref.
V-SBD-BET	Ni/Au	Ti/Al/Ni/Au	427 V	1.07	[133]
V-SBD-FP	Ni/Au	Ti/Au	730 V V	1.02	[139]
V-SBD-FPET	Ni/Au	Ti/Au	1722 V	1.03	[140]
L-SBD-FP	Ni/Au	Ti/Au	<3 kV	~1.25	[141]
L-SBD	Ni/Au	Ti/Au	1.7 kV	-	[142]
L-SBD	Pt	Ti/Au	-	1.40	[134]
L-SBD	Ir	Ti/Au	-	1.45	[134]
V-SBD	Ni	Ti/Au	-	1.57	[134]
L-SBD	Ni	Ti/Au	-	1.33	[134]
V-SBD	Cu	Ti/Au	-	1.53	[134]
L-SBD	W	Ti/Au	-	1.4	[134]
V-SBD	Ni/Au	Sn	~210 V	3.38	[143]
L-SBD	Ptx	Ti/Al/Au	-	-	[144]
V-SBD	Pt/Au	Ti/Au	-	-	[135]
V-SBD	TiN	Ti/Au	-	1.03	[145]
V-SBD	Pt/Ti/Au	Ti/Au	-	1.03	[136]
V-SBD-TCO	SnO/Ti	Ti/Au	-	1.09	[146]
V-MDS(TiO_2)	Ni/Au	Ti/Au	1010 V	-	[147]

In the counter-electrode, highly doped regions beneath the metallization are deployed to assist ohmicity of the contacts [139]. The dopants for this have previously been discussed. Another approach to this is using thin films of highly-conducting oxides [140].

Ohmic contacts to β-Ga_2O_3 are commonly based on Ti/Au, however other metal contacts have been utilized, such as In, Ti, Ti/Al/Au, In/Au, and Ti/Al/Ni/Au. Besides, there are other metals which have exhibited pseudo Ohmic behavior including Zr, Ag, and Sn [132]. This pseudo nature meant that, initially, ohmicity was observed but, after annealing, rectifying behavior became dominant. Therefore, the Schottky/Ohmic nature is also dependent upon the Ga_2O_3's surface/interface states together with the exact choice of metal stack, explaining, in turn, the varying contact resistivity of certain metals. While delivering low contact resistance, it is worth mentioning that Au is not considered a CMOS-compatible metal. This is an issue shared with GaN-based technology [148].

For the continued development of high voltage β-Ga_2O_3devices, edge termination is an important aspect as it is with its Si, GaN, and 4H-SiCcounterparts. Edge termination in β-$Ga_2O_3$is being explored and focused specifically on field plates (FP), imparted edge termination (ET), guard ring field plates, thermally oxidized termination, beveled mesas, and trench. These techniques are all deployed to further manage the electrical field to reduce the electric field crowding at the diode edges to increase its blocking capabilities. SBD devices can be made with either a vertical architecture, using homoepitaxial Ga_2O_3 or with a lateral architecture using either homo- or heteroepitaxial (e.g., on sapphire) Ga_2O_3. In general, the vertical structure is preferred as the device pitch is reduced and the encapsulation is simpler. Hu et al. [141] demonstrated a field-plated lateral β-Ga_2O_3 SBD on a sapphire substrate with a reverse blocking voltage of more than 3 kV, an R_{on}

of 24.3 mΩcm^2 (anode–cathode spacing 24 μm), and an FOM >0.37 GWcm^{-2} (while an FOM of ~500 GWcm^{-2} was achieved as the anode-cathode spacing (and V_{br}) was reduced). Zhou et al. [149] implemented a Mg implanted ET device on a vertical β-Ga_2O_3 SBD with a reverse blocking voltage of 1.55 kV and a low specific on-resistance of 5.1 mΩcm^2 (epi thickness 10 μm) and an FOM of 0.47 GWcm^{-2}. Analogously, Lin et al. [150] implemented a guard ring with or without an FP on vertical SBDs. The terminated devices exhibited a specific on-resistance of 4.7 mΩcm^2 and a V_{br} of 1.43 kV. Wang et al. [151] implemented a thermally oxidized termination on a vertical SBD with a V_{br} of 940 V, a specific on-resistance of 3.0 mΩcm^2, and an FOM of 0.295 GWcm^{-2}. Allen et al. [152] implemented a small-angle beveled field plate (SABFP), on thinned Ga_2O_3 substrates and a non-punch-through vertical SBD design rendering a V_{br} of 1100 V, a peak electric field of 3.5 MVcm^{-1}, and an FOM of 0.6 GWcm^{-2}.

Somehow the state of the art is given by Li et al. [153]. They demonstrated an FP vertical Ga_2O_3 trench SBDs with a V_{br} of 2.89 kV (which is ~500 V higher than those without FPs). The trench SBDs exhibited a differential specific on-resistance of 10.5 (8.8) mΩcm^2 from DC (pulsed) measurements leading to an FOM of 0.80 (0.95) GWcm^{-2}. This Baliga's power FOM is approaching that for the best vertical SBD GaN devices (e.g., 1.7 GWcm^{-2} [154]) but is still several times smaller than lateral AlGaN/GaN SBD (e.g., 3.6 GWcm^{-2} [155]) and bipolar *p-n* vertical GaN diodes (e.g., ~4.6 GWcm^{-2} [156]). Both, the 2D gas formed at the AlGaN/GaN interface and the bipolar injection are effective ways of further reducing the on-resistance in these devices while keeping the breakdown voltage high. The lack of low resistivity *p*-type layer for the anode has to date, prevented a competitive homojunction p-n Ga_2O_3 diode, but *p-n* heterojunction diodes have been realized by integrating *n*-type Ga_2O_3 with *p*-type semiconductors, such as CuO (1.49 kV) [157] and NiO (1.06 kV/1.86kV) [158,159]. Nickel oxide as the *p*-type blocking layer in heterojunction power diodes resulted in a particularly promising approach with this NiO/Ga_2O_3device [160] yielding a Baliga's FOM of 0.33 GWcm^{-2} (Figure 5c,d).

Recently, extremely high-*k* dielectrics have been explored for electric field management in WBG semiconductor-based lateral and vertical device structures [160–164]. According to the TCAD simulations of Roy et al. [165], a super-dielectric Ga_2O_3 SBD with practically achievable device dimensions with extremely high FOM should be possible; e.g., 20kVcanbeachievedforan R_{on} of 10 mΩ-cm^2 with a dielectric constant of 300, a Ga_2O_3 width/dielectric width ratio of 0.2, and an aspect ratio (drift layer length (anode to cathode spacing)/drift layer width ratio) of 10 resulting in a PFOM of 40 GWcm^{-2} (surpassing the theoretical unipolar FOM of β-Ga_2O_3SBD by four times).

3.5. Gallium Oxide Power Transistors

A power MOSFET fabrication process generally includes a number of technological steps including either gate dielectrics, surface passivation, drain/source ohmic contacts, implant doping, isolation, mesa etch, or in combination. Due to the large bandgap of Ga_2O_3, the most suitable gate insulators are those with enough (conduction and valence) band-offsets to avoid current injection through the gate (e.g., SiO_2 and Al_2O_3 and perhaps other oxides such as Y_2O_3, MgO, and Mg_2AlO_4). While balancing the dielectric constant to achieve more gate capacitance and more carriers in the conductive channel [166]. Defining a contact region by implantation, such as in Si, SiC, and GaN power MOSFET technologies, is a usual choice [167], in Ga_2O_3 this is typically n^+ Si-ion implantation. While other techniques have been suggested to further decrease the contact resistivity, such as formation of surface states [168] or the adoption of a TCO as a metallic interface [169].

As in, the more mature, AlGaN/GaN HEMT technology, Ohmic contacts are typically made with a multilayer metal stack consisting of an adhesion layer (e.g., Ti, Ta), an overlayer (Al), a barrier layer (e.g., Ni, Ti, Mo), and a capping of Au [170,171]. Nevertheless, it has been argued that simpler metal structures, such as Ti/Ga_2O_3, are also efficient if there is an oxygen deficient Ga_2O_3 surface [172] (a double charged oxygen vacancy is a well-known intrinsic donor in oxides [107]). Indeed, Yao et al. [132] suggested that the surface states

appear to have a more dominant role in the transformation from a Schottky to an Ohmic interface than the choice of metal.

As with power SBDs, power MOSFETs can be defined in a vertical Ga_2O_3 homoepitaxial structure (typical of SiC power MOSFETs) and lateral structure (typical of AlGaN/GaN power HEMTs) which can be either homoepitaxial or heteroepitaxial (Figure 6). Ga_2O_3 power MOSFETs are mostly unipolar *n*-type and operate in depletion mode (D-mode or normally-on) but a number of techniques have been reported to make enhancement mode (E-mode or normally-off) Ga_2O_3 devices. For example, Chabak et al. [173] reported an enhancement-mode β-Ga_2O_3 MOSFETs on a Si-doped homoepitaxial channel grown by molecular beam epitaxy and, using a gate recess process to partially remove the epitaxial channel under the 1-µm gated region to fully deplete at zero gate bias. With a breakdown voltage of 505 V (8 mm source-drain spacing), a maximum current density of 40 mA mm^{-1}, and an on/off ratio of 10^9. Hu et al. [174] achieved (in 2018) a larger blocking voltage (1.075 kV), a larger threshold voltage (1.2–2.2 V), and a larger output current (~500 A cm^{-2}) in a first demonstration of vertical E-mode MOSFET with significatively larger FOM (~80 MW cm^{-2}).

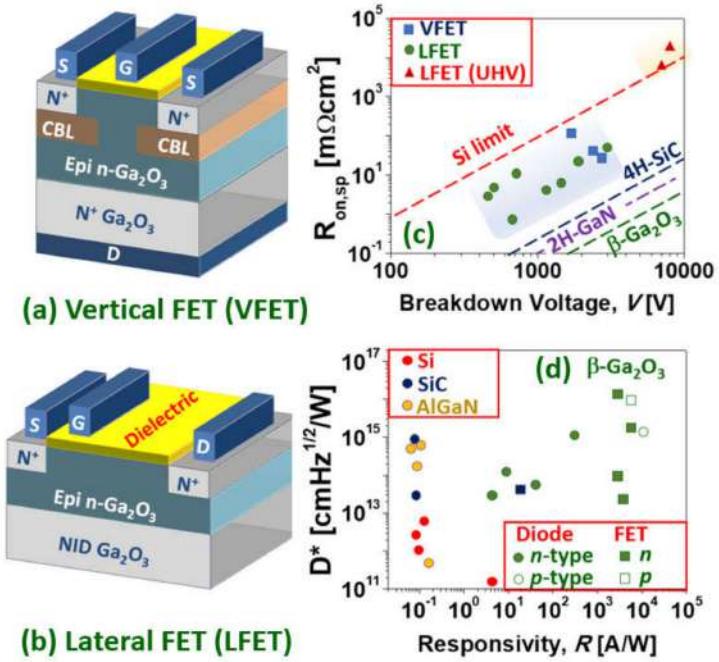

Figure 6. Schematics of (**a**) a vertical Ga_2O_3 power transistor (VFET) and (**b**) a lateral transistor (LFET). (**c**) Baliga's FOM for selected LFETs and VFETs from the literature. (**d**) Prospects of Ga_2O_3 devices as UV PDs, D* refers to specific detectivity; dots symbols referrer to diodes (either SBD or MSM), while square symbols denote transistors (data adapted from Wu et al. [131]). Adapted with permission from [12] © 2021 copyright Society of Photo-Optical Instrumentation Engineers (SPIE).

The E-mode was accomplished by doping profiling in a FinFET design (a type of 3D, non-planar transistor which has become the usual layout for the smallest CMOS 14 nm, 10 nm, and 7 nm nodes). This kind of E-mode vertical power device was later optimized to sustain up to a blocking voltage of 1.6kV [175], a threshold voltage of 2.66 kV, a maximum current density of 25.2 $mWcm^2$, and a record FOM of 280 MW cm^{-2} [176]. Among D-mode devices, the ones reported by Lv et al. [177] stand out for exhibiting a particularly large FOM. They reported (in 2019) [177] source-FP β-Ga_2O_3 MOSFETs on a Si-doped/Fe-doped semi-insulating β-Ga_2O_3 substrate exhibiting 222 mA mm^{-1} (18 mm source-drain spacing) with on-resistance of 11.7 $m\Omega cm^2$, a V_{br} of 680 V and an FOM of 50.4 $MWcm^{-2}$. Later (in 2020) [178], they adopted a T-shaped gate and source connected FP structure to increase the V_{br} up to 1.4 kV/2.9 kV (for 4.8 µm/17.8 µm source-drain spacing), with a specific on-resistances of 7.08 $m\Omega cm^2$/46.2 $m\Omega cm^2$. These yielded a record high FOM of

277 MW cm^{-2}, together with negligible gate or drain pulsed current collapse and a drain current on/off ratio of 10^9.

Other lateral D-mode devices with high FOM were reported by Tetzner et al. [179]. By using sub-μm gate lengths (combined with gate recess) and optimization of compensation-doped high-quality crystals, implantation based inter-device isolation, and SiNx-passivation, breakdown voltages of 1.8 kV and an FOM of 155 MW cm^{-2} were achieved. In 2020, Sharma et al. [180] reported Ga_2O_3 lateral D-mode field-plated MOSFETs exhibiting an ultra-high V_{br} of 8.03 kV (70 mm) by using polymer SU8 passivation. The current was rather low, however, due to plasma-induced damage of channel and access regions resulting in an impractical FOM of 7.73 kW cm^{-2} (i.e., not above the silicon limit). As reported by Kalarickal et al. [164], ultra-high-*k* ferroelectric dielectrics, such as $BaTiO_3$, can, in principle, provide an efficient field management strategy by improving the uniformity of electric field profile in the gate-drain region of lateral FETs. High average breakdown fields of 1.5 MV/cm (918 V) and 4 MVcm^{-1} (201 V) were demonstrated for gate-drain spacings of 6μm and 0.6 μm, respectively, in β-Ga_2O_3, at a high channel sheet charge density of 1.8×10^{13} cm^{-2}. An elevated sheet charge density together with a high breakdown field enabled a record power FOM of 376 MWcm^{-2} at a gate-drain spacing of 3 μm (Figure 6c). As in the case of SBDs, these performances for the Ga_2O_3 devices are already impressive and well beyond the silicon limit but still lag behind the best (much more mature) GaN devices in their respective power ratings [181,182].

All the above power MOSFET devices are unipolar *n*-type. These devices are sometimes referred as MISFETs so as to distinguish them from the conventional p-n junction based MOSFETs, since there are no *p*-regions in these MISFETs [175]. As mentioned in the previous sections, there are, however, several reports of *p*-type Ga_2O_3in nominally undoped, H-doped and N-doped β-Ga_2O_3. In particular, Wuetal. [131] proposed a growth mechanism of multistep structural phase transitions from hexagonal P63mc GaN to rhombohedral R3c α-$GaN_xO_{3(1-x)/2}$,and finally to monolithic C2/m N-doped β-Ga_2O_3. This improves the crystalline quality, facilitates acceptor doping, increases the acceptor activation efficiency, and thus enhances the *p*-type conductivity (acceptor ionization energy of 0.165 eV, Hall resistivity of 17.0 Ωcm, Hall hole mobility of 23.6 $cm^2V^{-1}s^{-1}$, hole concentration of 1.56×10^{16} cm^{-3}). P-type β-Ga_2O_3 films-based lateral MOSFET deep-ultraviolet (DUV) PDs were fabricated with extremely high responsivity (5.1×10^3 A/W) and detectivity (1.0×10^{16}Jones) under 250 nm light illumination (40 μW/cm^2) conditions. Figure 6d shows the responsivity and detectivity (D*) for state-of-the-art DUV PDs based on various WBG materials (adapted from [131]), in which it can be seen how β-Ga_2O_3 surpasses conventional Si-, SiC-, and AlGaN-based devices in terms of responsivity and detectivity.

4. Other Emerging Oxide Semiconductors for Power Electronics

Ga_2O_3phase engineering: Owing to the nonpolar nature of β-Ga_2O_3 crystals, modulation-doped heterostructure is one of the possible approaches to realize Ga_2O_3-based FETs [183]. Analogously, *p*-type semiconductors (e.g., *p*-type nitrides such as GaN) may be introduced to yield normally-off β-Ga_2O_3 field-effect transistors with tunable positive threshold voltages [184]. Other phases of Ga_2O_3 have also received attention due to potentially favorable growth characteristics, and to the possibility of polarization engineering made possible by the polar nature of their crystal structures. In principle, this polarization could be utilized to produce Ga_2O_3 two-dimensional electron gases (2DEGs) in analogy with GaN/AlN-based transistors [185].

Ga_2O_3alloy engineering: The aluminum gallium oxide, $Al_xGa_{1-x}O_3$, is a ternary alloy of Al_2O_3 and Ga_2O_3. It was already noted by Roy [186] in 1952 that the gallium ion closely resembles the aluminum ion and substitutes for it in several structures. Because β-$(AlGa)_2O_3$ is not the energetically favored crystalline phase for large Al compositions, the crystal converts to competing structural phases when grown on β-Ga_2O_3 substrates [187]. Thus, it has been difficult to obtain gallium oxide UWBG materials exceeding the bandgap of ~6 eV which is available to the materials in the nitride family in AlN. Very recently how-

ever, it was found that single-crystalline layers of α-$(AlGa)_2O_3$ alloys spanning bandgaps of 5.4–8.6 eV can be grown by molecular beam epitaxy [188]. By varying the alloy composition, bandgap energies from ~5.4 up to 8.6 eV with a bowing parameter of 1.1 eV are achieved, making α-$(Al_xGa_{1-x})_2O_3$ the largest bandgap epitaxial material family to date. If these layers can be controllably doped, it would pave the way for α-$(Al_xGa_{1-x})_2O_3$–based high-power heterostructure electronic and photonic devices at bandgaps far beyond all materials available today [189].

Spinel electronics: The spinel zinc gallate, $ZnGa_2O_4$, is a nearly stoichiometric mixed oxide made of Ga_2O_3 and ZnO.A potential advantage of spinel $ZnGa_2O_4$ is its great dopability prospects owing to the spinel's inherent diversity in cation coordination possibilities [106]. Normal spinels have all A cations in the tetrahedral site and all B cations in the octahedral site, e.g., Zn-tetrahedral site $Zn^{2+}(T_d)$ and Ga-octahedral site $Ga^{3+}(O_h)$, so that normal $ZnGa_2O_4$ is $Zn(^{2+}[T_d])Ga_2(^{3+}[O_h])O_4(^{2-})$. The spinel's off-stoichiometry, from the ideal 1:2:4 proportions, or the creation of cation antisite defects are known routes for doping these compounds. Dominant defects in spinels are antisite donors (e.g., Zn_{Ga}) or donor-like $Ga^{3+}(O_h)$-on-T_d and antisite acceptors (e.g., GaZn) with acceptor-like $Zn^{2+}(T_d)$-on-O_h antisite defects resulting in an intrinsic bipolar power semiconductor [190]. $ZnGa_2O_4$ is therefore a potential outstanding UWBG (~5 eV) oxide semiconductor but is only one among the many possible spinel oxides. There are over 1000 compounds that are known to crystalize in the spinel structure. The sub-family of spinel oxides is a large and important class of multi-functional oxide semiconductors with many optoelectronics applications in areas such as batteries, fuel cells, catalysis, photonics (phosphors, bio-imaging, photodetectors), spintronics (magnets, bio-magnets), or thermoelectricity [191]. Other magnesium-based Ga-spinels, such as $MgGa_2O_4$and $Zn_{1-x}Mg_xGa_2O_4$, are related oxides that are currently being investigated [192,193].

5. Conclusions

The rational use of electrical energy and information are central themes in the greatest climatic challenge of the 21st century. UWBG oxides, such as Ga_2O_3 and related materials, are promising power electronic candidates since their critical electric field is large compared to beyond silicon WBG (i.e., SiC and GaN), while still yielding a moderate mobility, high quality epi-layers, and large bulk single crystals (more than 6-inch) using low cost and scalable fabrication approaches. During the last decade, the Ga_2O_3 power diode and transistor progress has been impressive, with devices now approaching the frontier of the field. The material system also opens new optoelectronics avenues (owing its UVC spanning bandgap), and new electronics perspectives based on stabile interfaces and a natural integration with extremely high-*k* functional oxides. The advances offered by Ga_2O_3 are also opening the door to many more UWBG oxides (the largest family of wide bandgap semiconductors), such as the spinel, $ZnGa_2O_4$, along with many more that are anticipated. Therefore, the ever-increasing family of UWBG oxides is at the very frontier of a more efficient energy electronics which is adapted to tackle the 21st century climatic targets, although there still is a lot of room for performance improvements, technical innovation, and new discoveries.

Author Contributions: Conceptualization A.P.-T., E.C., M.R.J.; writing—original draft preparation, A.P.-T., Z.C., J.J.A.; writing—review and editing, A.P.-T., Z.C., J.J.A.; visualization, A.P.-T.; supervision, A.P.-T.; project administration, A.P.-T.; funding acquisition, E.C., A.P.-T., M.R.J. All authors have read and agreed to the published version of the manuscript.

Funding: This research was funded by the French National Research Agency ANR, "Accelerating the demonstration of Gallium Oxide's outstanding potential for Energy application" (GOPOWER), grant number Project-ANR-21-CE50-0015.

Institutional Review Board Statement: Not applicable.

Informed Consent Statement: Not applicable.

Data Availability Statement: Not applicable.

Acknowledgments: Authors acknowledge IRP -"GALLIA", CNRS, France. The ICN2 is funded by the CERCA programme/Generalitat de Catalunya. The ICN2 is supported by the Severo Ochoa Centres of Excellence programme, funded by the Spanish Research Agency (AEI, grant no. SEV-2017-0706).

Conflicts of Interest: The authors declare no conflict of interest.

References

1. IPCC Working Group I Report, Climate Change 2021: The Physical Science Basis. Available online: www.ipcc.ch (accessed on 9 August 2021).
2. US Environmental Protection Agency (EPA). Greenhouse Gas Emissions: Global Greenhouse Gas Emissions Data. 2021. Available online: https://www.epa.gov/ghgemissions/global-greenhouse-gas-emissions-data (accessed on 6 November 2017).
3. Leo Lorenz, Power Device Development Trends—From Silicon to Wide Bandgap? Available online: www.power-and-beyond.com (accessed on 16 December 2021).
4. Pearton, S.J.; Ren, F.; Tadjer, M.; Kim, J. Perspective: Ga_2O_3 for ultra-high power rectifiers and MOSFETS. *J. Appl. Phys.* **2018**, *124*, 220901. [CrossRef]
5. Reese, S.B.; Remo, T.; Green, J.; Zakutayev, A. How Much Will Gallium Oxide Power Electronics Cost? *Joule* **2019**, *3*, 903–907. [CrossRef]
6. Chu, S.; Cui, Y.; Liu, N. The path towards sustainable energy. *Nat. Mater.* **2017**, *16*, 16–22. [CrossRef] [PubMed]
7. Millan, J.; Godignon, P.; Perpiñà, X.; Perez-Tomas, A.; Rebollo, J. A Survey of Wide Bandgap Power Semiconductor Devices. *IEEE Trans. Power Electron.* **2013**, *29*, 2155–2163. [CrossRef]
8. Spaziani, L.; Lu, L. Silicon, GaN and SiC: There's room for all: An application space overview of device considerations. In Proceedings of the 2018 IEEE 30th International Symposium on Power Semiconductor Devices and ICs (ISPSD), Chicago, IL, USA, 13–17 May 2018; pp. 8–11.
9. Jones, E.A.; Wang, F.F.; Costinett, D. Review of Commercial GaN Power Devices and GaN-Based Converter Design Challenges. *IEEE J. Emerg. Sel. Top. Power Electron.* **2016**, *4*, 707–719. [CrossRef]
10. Tsao, J.Y.; Chowdhury, S.; Hollis, M.A.; Jena, D.; Johnson, N.M.; Jones, K.A.; Kaplar, R.J.; Rajan, S.; Van de Walle, C.G.; Bellotti, E.; et al. Ultrawide-Bandgap Semiconductors: Research Opportunities and Challenges. *Adv. Electron. Mater.* **2017**, *4*, 1600501. [CrossRef]
11. Perez-Tomas, A.; Teherani, F.H.; Bove, P.; Sandana, E.V.; Chikoidze, E.; Jennings, M.R.; Rogers, D.J.; Russell, S.A.O. Wide and ultra-wide bandgap oxides: Where paradigm-shift photovoltaics meets transparent power electronics. In Proceedings of the SPIE 10533, Oxide-Based Materials and Devices IX, San Francisco, CA, USA, 27 January–1 February 2018. [CrossRef]
12. Perez-Tomas, A.; Chikoidze, E.; Rogers, D.J. A walk on the frontier of energy electronics with power ultra-wide bandgap oxides and ultra-thin neuromorphic 2D materials. In Proceedings of the SPIE 11687, Oxide-Based Materials and Devices XII, San Francisco, CA, USA, 6–12 March 2021. [CrossRef]
13. Perez-Tomas, A.; Lodzinski, M.; Guy, O.J.; Jennings, M.R.; Placidi, M.; Llobet, J.; Gammon, P.M.; Davis, M.C.; Covington, J.A.; Burrows, S.E.; et al. Si/SiC bonded wafer: A route to carbon free SiO_2 on SiC. *Appl. Phys. Lett.* **2009**, *94*, 103510. [CrossRef]
14. Nawaz, M. Introductory Chapter: Earth Crust-Origin, Structure, Composition and Evolution. In *Earth Crust*; IntechOpen: London, UK, 2019. [CrossRef]
15. Jackson, I. *The Earth's Mantle—Composition, Structure and Evolution*; Cambridge University Press: Cambridge, UK, 1998.
16. Higashiwaki, M.; Sasaki, K.; Murakami, H.; Kumagai, Y.; Koukitu, A.; Kuramata, A.; Masui, T.; Yamakoshi, S. Recent progress in Ga_2O_3 power devices. *Semicond. Sci. Technol.* **2016**, *31*, 034001. [CrossRef]
17. Kuramata, A.; Koshi, K.; Watanabe, S.; Yamaoka, Y.; Masui, T.; Yamakoshi, S. Bulk crystal growth of Ga_2O_3. In Proceedings of the SPIE 10533, Oxide-Based Materials and Devices IX, San Francisco, CA, USA, 27 January–1 February 2018. [CrossRef]
18. Playford, H.Y.; Hannon, A.C.; Barney, E.R.; Walton, R.I. Structures of Uncharacterised Polymorphs of Gallium Oxide from Total Neutron Diffraction. *Chem. A Eur. J.* **2013**, *19*, 2803–2813. [CrossRef]
19. Geller, S. Crystal Structure of β—Ga_2O_3. *J. Chem. Phys.* **1960**, *33*, 676–684. [CrossRef]
20. Blasse, G.; Bril, A. Some observations on the luminescence of β-Ga_2O_3. *J. Phys. Chem. Solids* **1970**, *31*, 707–711. [CrossRef]
21. Lorenz, M.; Woods, J.; Gambino, R. Some electrical properties of the semiconductor β Ga_2O_3. *J. Phys. Chem. Solids* **1967**, *28*, 403–404. [CrossRef]
22. Tippins, H.H. Optical Absorption and Photoconductivity in the Band Edge of β−Ga_2O_3. *Phys. Rev.* **1965**, *140*, A316–A319. [CrossRef]
23. Nouketcha, F.L.L.; Cui, Y.; Lelis, A.; Green, R.; Darmody, C.; Schuster, J.; Goldsman, N. Investigation of Wide- and Ultrawide-Bandgap Semiconductors From Impact-Ionization Coefficients. *IEEE Trans. Electron. Devices* **2020**, *67*, 3999–4005. [CrossRef]
24. Chikoidze, E.; Tchelidze, T.; Sartel, C.; Chi, Z.; Kabouche, R.; Madaci, I.; Rubio, C.; Mohamed, H.; Sallet, V.; Medjdoub, F.; et al. Ultra-high critical electric field of 13.2 MV/cm for Zn-doped p-type β-Ga_2O_3. *Mater. Today Phys.* **2020**, *15*, 100263. [CrossRef]
25. Baliga, B. Power semiconductor device figure of merit for high-frequency applications. *IEEE Electron Device Lett.* **1989**, *10*, 455–457. [CrossRef]

26. Ma, N.; Tanen, N.; Verma, A.; Guo, Z.; Luo, T.; Xing, H.; Jena, D. Intrinsicelectronmobilitylimits in β-Ga_2O_3. *Appl. Phys. Lett.* **2016**, *109*, 212101. [CrossRef]
27. Fu, B.; Jia, Z.; Mu, W.; Yin, Y.; Zhang, J.; Tao, X. A review of β-Ga_2O_3 single crystal defects, their effects on device performance and their formation mechanism. *J. Semicond.* **2019**, *40*, 011804. [CrossRef]
28. Stuchlikova, T.H.; Stuchlik, J.; Remes, Z.; Taylor, A.; Mortet, V.; Ashcheulov, P.; Gregora, I.; Krivyakin, G.; Volodin, V. High-Temperature PIN Diodes Based on Amorphous Hydrogenated Silicon-Carbon Alloys and Boron-Doped Diamond Thin Films. *Phys. Status Solidi* **2020**, *257*, 1900247. [CrossRef]
29. Chase, A.O. Growth of beta-Ga_2, O_3 by the Verneuil Technique. *J. Am. Ceram. Soc.* **1964**, *47*, 470. [CrossRef]
30. Galazka, Z.; Ganschow, S.; Irmscher, K.; Klimm, D.; Albrecht, M.; Schewski, R.; Pietsch, M.; Schulz, T.; Dittmar, A.; Kwasniewski, A.; et al. Bulk single crystals of β-Ga_2O_3 and Ga-based spinels as ultra-wide bandgap transparent semiconducting oxides. *Prog. Cryst. Growth Charact. Mater.* **2020**, *67*, 100511. [CrossRef]
31. Galazka, Z.; Irmscher, K.; Schewski, R.; Hanke, I.M.; Pietsch, M.; Ganschow, S.; Klimm, D.; Dittmar, A.; Fiedler, A.; Schroeder, T.; et al. Czochralski-grown bulk β-Ga_2O_3 single crystals doped with mono-, di-, tri-, and tetravalent ions. *J. Cryst. Growth* **2019**, *529*, 125297. [CrossRef]
32. Galazka, Z.; Schewski, R.; Irmscher, K.; Drozdowski, W.; Witkowski, M.E.; Makowski, M.; Wojtowicz, A.J.; Hanke, I.M.; Pietsch, M.; Schulz, T.; et al. Bulk β-Ga_2O_3 single crystals doped with Ce, Ce+Si, Ce+Al, and Ce+Al+Si for detection of nuclear radiation. *J. Alloys Compd.* **2019**, *818*, 152842. [CrossRef]
33. Irmscher, K.; Galazka, Z.; Pietsch, M.; Uecker, R.; Fornari, R. Electrical properties of β-Ga_2O_3 single crystals grown by the Czochralski method. *J. Appl. Phys.* **2011**, *110*, 063720. [CrossRef]
34. Víllora, E.G.; Shimamura, K.; Yoshikawa, Y.; Aoki, K.; Ichinose, N. Large-size β-Ga_2O_3 single crystals and wafers. *J. Cryst. Growth* **2004**, *270*, 420–426. [CrossRef]
35. Hoshikawa, K.; Kobayashi, T.; Matsuki, Y.; Ohba, E. 2-inch diameter (1 0 0) β-Ga_2O_3 crystal growth by the vertical Bridgman technique in a resistance heating furnace in ambient air. *J. Cryst. Growth* **2020**, *545*, 125724. [CrossRef]
36. Hoshikawa, K.; Ohba, E.; Kobayashi, T.; Yanagisawa, J.; Miyagawa, C.; Nakamura, Y. Growth of β-Ga_2O_3 single crystals using vertical Bridgman method in ambient air. *J. Cryst. Growth* **2016**, *447*, 36–41. [CrossRef]
37. Harwig, T.; Schoonman, J. Electrical properties of β-Ga_2O_3 single crystals. II. *J. Solid State Chem.* **1978**, *23*, 205–211. [CrossRef]
38. Cui, H.; Mohamed, H.; Xia, C.; Sai, Q.; Zhou, W.; Qi, H.; Zhao, J.; Si, J.; Ji, X. Tuning electrical conductivity of β-Ga_2O_3 single crystals by Ta doping. *J. Alloys Compd.* **2019**, *788*, 925–928. [CrossRef]
39. Hossain, E.; Kulkarni, R.; Mondal, R.; Guddolian, S.; Rahman, A.A.; Thamizhavel, A.; Bhattacharya, A. Optimization of Gas Ambient for High Quality β-Ga_2O_3 Single Crystals Grown by the Optical Floating Zone Technique. *ECS J. Solid State Sci. Technol.* **2019**, *8*, Q3144–Q3148. [CrossRef]
40. Suzuki, N.; Ohira, S.; Tanaka, M.; Sugawara, T.; Nakajima, K.; Shishido, T. Fabrication and characterization of transparent conductive Sn-doped β-Ga_2O_3 single crystal. *Phys. Status Solidi* **2007**, *4*, 2310–2313. [CrossRef]
41. Tomioka, Y.; Ozaki, Y.; Inaba, H.; Ito, T. Compensation effects between impurity cations in single crystals of a wide gap semiconductor β-Ga_2O_3 prepared by the floating zone method. *Jpn. J. Appl. Phys.* **2019**, *58*, 091009. [CrossRef]
42. Zhou, W.; Xia, C.; Sai, Q.; Zhang, H. Controlling n-type conductivity of β-Ga_2O_3 by Nb doping. *Appl. Phys. Lett.* **2017**, *111*, 242103. [CrossRef]
43. Galazka, Z. β-Ga_2O_3 for wide-bandgap electronics and optoelectronics. *Semicond. Sci. Technol.* **2018**, *33*, 113001. [CrossRef]
44. Galazka, Z.; Uecker, R.; Klimm, D.; Irmscher, K.; Naumann, M.; Pietsch, M.; Kwasniewski, A.; Bertram, R.; Ganschow, S.; Bickermann, M. Scaling-Up of Bulk β-Ga_2O_3Single Crystals by the Czochralski Method. *ECS J. Solid State Sci. Technol.* **2016**, *6*, Q3007–Q3011. [CrossRef]
45. Saleh, M.; Varley, J.B.; Jesenovec, J.; Bhattacharyya, A.; Krishnamoorthy, S.; Swain, S.; Lynn, K.G. Degenerate doping in β-Ga_2O_3 single crystals through Hf-doping. *Semicond. Sci. Technol.* **2020**, *35*, 04LT01. [CrossRef]
46. Kuramata, A.; Koshi, K.; Watanabe, S.; Yamaoka, Y.; Masui, T.; Yamakoshi, S. High-quality β-Ga_2O_3single crystals grown by edge-defined film-fed growth. *Jpn. J. Appl. Phys.* **2016**, *55*, 1202A2. [CrossRef]
47. Yao, Y.; Sugawara, Y.; Ishikawa, Y. Identification of Burgers vectors of dislocations in monoclinic β-Ga_2O_3 via synchrotron X-ray topography. *J. Appl. Phys.* **2020**, *127*, 205110. [CrossRef]
48. Hoshikawa, K.; Kobayashi, T.; Ohba, E. 50 mm diameter Sn-doped (0 0 1) β-Ga_2O_3 crystal growth using the vertical Bridgeman technique in ambient air. *J. Cryst. Growth* **2020**, *546*, 125778. [CrossRef]
49. Aubay, E.; Gourier, D. Magnetic bistability and Overhauser shift of conduction electrons in gallium oxide. *Phys. Rev. B* **1993**, *47*, 15023–15036. [CrossRef]
50. He, N.; Tang, H.; Liu, B.; Zhu, Z.; Li, Q.; Guo, C.; Gu, M.; Xu, J.; Liu, J.; Xu, M.; et al. Ultra-fast scintillation properties of β-Ga_2O_3 single crystals grown by Floating Zone method. *Nucl. Instrum. Methods Phys. Res. Sect. A Accel. Spectrom. Detect. Assoc. Equip.* **2018**, *888*, 9–12. [CrossRef]
51. Usui, Y.; Oya, T.; Okada, G.; Kawaguchi, N.; Yanagida, T. Comparative study of scintillation and optical properties of Ga_2O_3 doped with ns2 ions. *Mater. Res. Bull.* **2017**, *90*, 266–272. [CrossRef]
52. Yanagida, T.; Kawaguchi, N. Optical and scintillation properties of alkaline earth doped Ga_2O_3 single crystals prepared by the floating zone method. *Jpn. J. Appl. Phys.* **2019**, *59*, SCCB20. [CrossRef]

53. Zhang, S.; Lian, X.; Ma, Y.; Liu, W.; Zhang, Y.; Xu, Y.; Cheng, H. Growth and characterization of 2-inch high quality β-Ga_2O_3 single crystals grown by EFG method. *J. Semicond.* **2018**, *39*, 083003. [CrossRef]
54. Oshima, T.; Hashiguchi, A.; Moribayashi, T.; Koshi, K.; Sasaki, K.; Kuramata, A.; Ueda, O.; Oishi, T.; Kasu, M. Electrical properties of Schottky barrier diodes fabricated on (001) β-Ga_2O_3substrates with crystal defects. *Jpn. J. Appl. Phys.* **2017**, *56*, 86501. [CrossRef]
55. Oshima, Y.; V́llora, E.G.; Shimamura, K. Quasi-heteroepitaxial growth of β-Ga_2O_3 on off-angled sapphire (0 0 0 1) substrates by halide vapor phase epitaxy. *J. Cryst. Growth* **2015**, *410*, 53–58. [CrossRef]
56. Xiong, Z.-N.; Xiu, X.-Q.; Li, Y.-W.; Hua, X.-M.; Xie, Z.-L.; Chen, P.; Liu, B.; Han, P.; Zhang, R.; Zheng, Y.-D. Growth of β -Ga_2O_3 Films on Sapphire by Hydride Vapor Phase Epitaxy. *Chin. Phys. Lett.* **2018**, *35*, 058101. [CrossRef]
57. Yao, Y.; Lyle, L.A.M.; Rokholt, J.A.; Okur, S.; Tompa, G.S.; Salagaj, T.; Sbrockey, N.; Davis, R.F.; Porter, L.M. (Invited) Growth and Characterization of α-,β-, and ε-Ga_2O_3 Epitaxial Layers on Sapphire. *ECS Trans.* **2017**, *80*, 191–196. [CrossRef]
58. Xiu, X.; Zhang, L.; Li, Y.; Xiong, Z.; Zhang, R.; Zheng, Y. Application of halide vapor phase epitaxy for the growth of ultra-wide band gap Ga_2O_3. *J. Semicond.* **2019**, *40*, 011805. [CrossRef]
59. Modak, S.; Chernyak, L.; Khodorov, S.; Lubomirsky, I.; Yang, J.; Ren, F.; Pearton, S.J. Impact of Electron Injection and Temperature on Minority Carrier Transport in Alpha-Irradiated ß-Ga_2O_3 Schottky Rectifiers. *ECS J. Solid State Sci. Technol.* **2019**, *8*, Q3050–Q3053. [CrossRef]
60. De Santi, C.; Nardo, A.; Wong, M.; Goto, K.; Kuramata, A.; Yamakoshi, S.; Murakami, H.; Kumagai, Y.; Higashiwaki, M.; Meneghesso, G.; et al. Stability and degradation of isolation and surface in Ga_2O_3 devices. *Microelectron. Reliab.* **2019**, *100–101*, 113453. [CrossRef]
61. Leach, J.H.; Udwary, K.; Rumsey, J.; Dodson, G.; Splawn, H.; Evans, K.R. Halide vapor phase epitaxial growth of β-Ga_2O_3 and α-Ga_2O_3 films. *APL Mater.* **2019**, *7*, 022504. [CrossRef]
62. Murakami, H.; Nomura, K.; Goto, K.; Sasaki, K.; Kawara, K.; Thieu, Q.T.; Togashi, R.; Kumagai, Y.; Higashiwaki, M.; Kuramata, A.; et al. Homoepitaxial growth of β-Ga_2O_3layers by halide vapor phase epitaxy. *Appl. Phys. Express* **2014**, *8*, 015503. [CrossRef]
63. Bin Anooz, S.; Grüneberg, R.; Wouters, C.; Schewski, R.; Albrecht, M.; Fiedler, A.; Irmscher, K.; Galazka, Z.; Miller, W.; Wagner, G.; et al. Step flow growth of β-Ga_2O_3 thin films on vicinal (100) β-Ga_2O_3 substrates grown by MOVPE. *Appl. Phys. Lett.* **2020**, *116*, 182106. [CrossRef]
64. Bin Anooz, S.; Grüneberg, R.; Chou, T.-S.; Fiedler, A.; Irmscher, K.; Wouters, C.; Schewski, R.; Albrecht, M.; Galazka, Z.; Miller, W.; et al. Impact of chamber pressure and Si-doping on the surface morphology and electrical properties of homoepitaxial (100) β-Ga_2O_3 thin films grown by MOVPE. *J. Phys. D Appl. Phys.* **2020**, *54*, 034003. [CrossRef]
65. Gogova, D.; Schmidbauer, M.; Kwasniewski, A. Homo- and heteroepitaxial growth of Sn-doped β-Ga_2O_3 layers by MOVPE. *CrystEngComm* **2015**, *17*, 6744–6752. [CrossRef]
66. Albrecht, M.; Schewski, R.; Wouters, C.; Fielder, A.; Irmscher, K.; Galazka, Z.; Popp, A.; Anooz, S.B.; Baldini, M.; Wagner, G. Ga_2O_3 from Materials to Devices. *Appl. Phys. Res.* **2021**, *5*, 011301.
67. Baldini, M.; Albrecht, M.; Fiedler, A.; Irmscher, K.; Schewski, R.; Wagner, G. Editors' Choice—Si- and Sn-Doped Homoepitaxial β-Ga_2O_3 Layers Grown by MOVPE on (010)-Oriented Substrates. *ECS J. Solid State Sci. Technol.* **2016**, *6*, Q3040–Q3044. [CrossRef]
68. Cui, R.-R.; Zhang, J.; Luo, Z.-J.; Guo, X.; Ding, Z.; Deng, C.-Y. Microstructure, optical, and photoluminescence properties of β-Ga_2O_3 films prepared by pulsed laser deposition under different oxygen partial pressures. *Chin. Phys. B* **2021**, *30*, 028505. [CrossRef]
69. Leedy, K.; Chabak, K.D.; Vasilyev, V.; Look, D.C.; Boeckl, J.J.; Brown, J.L.; Tetlak, S.E.; Green, A.J.; Moser, N.A.; Crespo, A.; et al. Highly conductive homoepitaxial Si-doped Ga_2O_3 films on (010) β-Ga_2O_3 by pulsed laser deposition. *Appl. Phys. Lett.* **2017**, *111*, 012103. [CrossRef]
70. Shen, H.; Baskaran, K.; Yin, Y.; Tian, K.; Duan, L.; Zhao, X.; Tiwari, A. Effect of thickness on the performance of solar blind photodetectors fabricated using PLD grown β-Ga_2O_3 thin films. *J. Alloys Compd.* **2019**, *822*, 153419. [CrossRef]
71. Vu, T.K.O.; Lee, D.U.; Kim, E.K. The effect of oxygen partial pressure on band gap modulation of Ga_2O_3 grown by pulsed laser deposition. *J. Alloys Compd.* **2019**, *806*, 874–880. [CrossRef]
72. Pearton, S.J.; Yang, J.; Cary, P.H., IV; Ren, F.; Kim, J.; Tadjer, M.J.; Mastro, M.A. A review of Ga_2O_3 materials, processing, and devices. *Appl. Phys. Rev.* **2018**, *5*, 011301. [CrossRef]
73. Chen, Z.; Wang, X.; Zhang, F.; Noda, S.; Saito, K.; Tanaka, T.; Nishio, M.; Guo, Q. Temperature dependence of luminescence spectra in europium doped Ga_2O_3 film. *J. Lumin.* **2016**, *177*, 48–53. [CrossRef]
74. Wang, Q.; Chen, J.; Huang, P.; Li, M.; Lu, Y.; Homewood, K.P.; Chang, G.; Chen, H.; He, Y. Influence of growth temperature on the characteristics of β-Ga_2O_3 epitaxial films and related solar-blind photodetectors. *Appl. Surf. Sci.* **2019**, *489*, 101–109. [CrossRef]
75. Yadav, M.K.; Mondal, A.; Das, S.; Sharma, S.; Bag, A. Impact of annealing temperature on band-alignment of PLD grown Ga_2O_3/Si (100) heterointerface. *J. Alloys Compd.* **2019**, *819*, 153052. [CrossRef]
76. Yu, J.; Nie, Z.; Dong, L.; Yuan, L.; Li, D.; Huang, Y.; Zhang, L.; Zhang, Y.; Jia, R. Influence of annealing temperature on structure and photoelectrical performance of β-Ga_2O_3/4H-SiC heterojunction photodetectors. *J. Alloys Compd.* **2019**, *798*, 458–466. [CrossRef]
77. Puurunen, R.L. A Short History of Atomic Layer Deposition: Tuomo Suntola's Atomic Layer Epitaxy. *Chem. Vap. Depos.* **2014**, *20*, 332–344. [CrossRef]
78. Siah, S.C.; Brandt, R.E.; Lim, K.; Schelhas, L.T.; Jaramillo, R.; Heinemann, M.D.; Chua, D.; Wright, J.; Perkins, J.D.; Segre, C.U.; et al. Dopant activation in Sn-doped Ga_2O_3 investigated by X-ray absorption spectroscopy. *Appl. Phys. Lett.* **2015**, *107*, 252103. [CrossRef]

79. Choi, D.-W.; Chung, K.-B.; Park, J.-S. Low temperature Ga_2O_3 atomic layer deposition using gallium tri-isopropoxide and water. *Thin Solid Films* **2013**, *546*, 31–34. [CrossRef]
80. Mizutani, F.; Higashi, S.; Inoue, M.; Nabatame, T. Atomic layer deposition of high purity Ga_2O_3 films using liquid pentamethylcyclopentadienyl gallium and combinations of H_2O and O_2 plasma. *J. Vac. Sci. Technol. A* **2020**, *38*, 022412. [CrossRef]
81. Ilhom, S.; Mohammad, A.; Shukla, D.; Grasso, J.; Willis, B.G.; Okyay, A.K.; Biyikli, N. Low-Temperature As-Grown Crystalline β-Ga_2O_3 Films via Plasma-Enhanced Atomic Layer Deposition. *ACS Appl. Mater. Interfaces* **2021**, *13*, 8538–8551. [CrossRef]
82. Jiao, Y.; Jiang, Q.; Meng, J.; Zhao, J.; Yin, Z.; Gao, H.; Zhang, J.; Deng, J.; Zhang, X. Growth and characteristics of β-Ga_2O_3 thin films on sapphire (0001) by low pressure chemical vapour deposition. *Vacuum* **2021**, *189*, 110253. [CrossRef]
83. Tao, J.; Lu, H.-L.; Gu, Y.; Ma, H.-P.; Li, X.; Chen, J.-X.; Liu, W.-J.; Zhang, H.; Feng, J.-J. Investigation of growth characteristics, compositions, and properties of atomic layer deposited amorphous Zn-doped Ga_2O_3 films. *Appl. Surf. Sci.* **2019**, *476*, 733–740. [CrossRef]
84. Sasaki, K.; Higashiwaki, M.; Kuramata, A.; Masui, T.; Yamakoshi, S. MBE grown Ga_2O_3 and its power device applications. *J. Cryst. Growth* **2013**, *378*, 591–595. [CrossRef]
85. Mazzolini, P.; Falkenstein, A.; Wouters, C.; Schewski, R.; Markurt, T.; Galazka, Z.; Martin, M.; Albrecht, M.; Bierwagen, O. Substrate-orientation dependence of β-Ga_2O_3 (100), (010), (001), and ($2^{-}01$) homoepitaxy by indium-mediated metal-exchange catalyzed molecular beam epitaxy (MEXCAT-MBE). *APL Mater.* **2020**, *8*, 011107. [CrossRef]
86. Nepal, N.; Katzer, D.S.; Downey, B.P.; Wheeler, V.D.; Nyakiti, L.O.; Storm, D.F.; Hardy, M.T.; Freitas, J.A.; Jin, E.N.; Vaca, D.; et al. Heteroepitaxial growth of β-Ga_2O_3 films on SiC via molecular beam epitaxy. *J. Vac. Sci. Technol. A Vac. Surf. Films* **2020**, *38*, 063406. [CrossRef]
87. Kamimura, T.; Nakata, Y.; Higashiwaki, M. Effect of $(AlGa)_2O_3$ back barrier on device characteristics of β-Ga_2O_3 metal-oxide-semiconductor field-effect transistors with Si-implanted channel. *Jpn. J. Appl. Phys.* **2021**, *60*, 030906. [CrossRef]
88. Mazzolini, P.; Vogt, P.; Schewski, R.; Wouters, C.; Albrecht, M.; Bierwagen, O. Faceting and metal-exchange catalysis in (010) β-Ga_2O_3 thin films homoepitaxially grown by plasma-assisted molecular beam epitaxy. *APL Mater.* **2019**, *7*, 022511. [CrossRef]
89. Ngo, T.S.; Le, D.D.; Lee, J.; Hong, S.-K.; Ha, J.-S.; Lee, W.-S.; Moon, Y.-B. Investigation of defect structure in homoepitaxial ($2^{-}01$) β-Ga_2O_3 layers prepared by plasma-assisted molecular beam epitaxy. *J. Alloys Compd.* **2020**, *834*, 155027. [CrossRef]
90. Ahmadi, E.; Koksaldi, O.S.; Kaun, S.W.; Oshima, Y.; Short, D.B.; Mishra, U.K.; Speck, J.S. Ge doping of β-Ga_2O_3 films grown by plasma-assisted molecular beam epitaxy. *Appl. Phys. Express* **2017**, *10*, 041102. [CrossRef]
91. Cheng, Y.; Xu, Y.; Li, Z.; Zhang, J.; Chen, D.; Feng, Q.; Xu, S.; Zhou, H.; Zhang, J.; Hao, Y.; et al. Heteroepitaxial growth of α-Ga_2O_3 thin films on a-, c- and r-plane sapphire substrates by low-cost mist-CVD method. *J. Alloys Compd.* **2020**, *831*, 154776. [CrossRef]
92. Kaneko, K.; Fujita, S.; Hitora, T. A power device material of corundum-structured α-Ga_2O_3fabricated by MIST EPITAXY®® technique. *Jpn. J. Appl. Phys.* **2018**, *57*, 02CB18. [CrossRef]
93. Ma, T.; Chen, X.; Ren, F.; Zhu, S.; Gu, S.; Zhang, R.; Zheng, Y.; Ye, J. Heteroepitaxial growth of thick α-Ga_2O_3 film on sapphire (0001) by MIST-CVD technique. *J. Semicond.* **2019**, *40*, 012804. [CrossRef]
94. Morimoto, S.; Nishinaka, H.; Yoshimoto, M. Growth and characterization of F-doped α-Ga_2O_3 thin films with low electrical resistivity. *Thin Solid Films* **2019**, *682*, 18–23. [CrossRef]
95. Isomura, N.; Nagaoka, T.; Watanabe, Y.; Kutsuki, K.; Nishinaka, H.; Yoshimoto, M. Determination of Zn-containing sites in β-Ga_2O_3 film grown through mist chemical vapor deposition via X-ray absorption spectroscopy. *Jpn. J. Appl. Phys.* **2020**, *59*, 070909. [CrossRef]
96. Nishinaka, H.; Nagaoka, T.; Kajita, Y.; Yoshimoto, M. Rapid homoepitaxial growth of (010) β-Ga_2O_3 thin films via mist chemical vapor deposition. *Mater. Sci. Semicond. Process.* **2021**, *128*, 105732. [CrossRef]
97. Xu, Y.; Cheng, Y.; Li, Z.; Chen, D.; Xu, S.; Feng, Q.; Zhu, W.; Zhang, Y.; Zhang, J.; Zhang, C.; et al. Ultrahigh-Performance Solar-Blind Photodetectors Based on High Quality Heteroepitaxial Single Crystalline β-Ga_2O_3 Film Grown by Vacuumfree, Low-Cost Mist Chemical Vapor Deposition. *Adv. Mater. Technol.* **2021**, *6*, 2001296. [CrossRef]
98. Lee, S.-D.; Kaneko, K.; Fujita, S. Homoepitaxial growth of beta gallium oxide films by mist chemical vapor deposition. *Jpn. J. Appl. Phys.* **2016**, *55*, 1202B8. [CrossRef]
99. Li, Z.; Jiao, T.; Yu, J.; Hu, D.; Lv, Y.; Li, W.; Dong, X.; Zhang, B.; Zhang, Y.; Feng, Z.; et al. Single crystalline β-Ga_2O_3 homoepitaxial films grown by MOCVD. *Vacuum* **2020**, *178*, 109440. [CrossRef]
100. Feng, Z.; Bhuiyan, A.F.M.A.U.; Karim, R.; Zhao, H. MOCVD homoepitaxy of Si-doped (010) β-Ga_2O_3 thin films with superior transport properties. *Appl. Phys. Lett.* **2019**, *114*, 250601. [CrossRef]
101. Zhang, Y.; Alema, F.; Mauze, A.; Koksaldi, O.S.; Miller, R.; Osinsky, A.; Speck, J.S. MOCVD grown epitaxial β-Ga_2O_3 thin film with an electron mobility of 176 cm2/V s at room temperature. *APL Mater.* **2019**, *7*, 022506. [CrossRef]
102. Alema, F.; Hertog, B.; Osinsky, A.; Mukhopadhyay, P.; Toporkov, M.; Schoenfeld, W.V. Fast growth rate of epitaxial β–Ga_2O_3 by close coupled showerhead MOCVD. *J. Cryst. Growth* **2017**, *475*, 77–82. [CrossRef]
103. Li, Z.; Jiao, T.; Hu, D.; Lv, Y.; Li, W.; Dong, X.; Zhang, Y.; Feng, Z.; Zhang, B. Study on β-Ga_2O_3 Films Grown with Various VI/III Ratios by MOCVD. *Coatings* **2019**, *9*, 281. [CrossRef]
104. Tadjer, M.J.; Alema, F.; Osinsky, A.; Mastro, M.A.; Nepal, N.; Woodward, J.M.; Myers-Ward, R.L.; Glaser, E.R.; Freitas, J.A.; Jacobs, A.G.; et al. Characterization of β-Ga_2O_3 homoepitaxial films and MOSFETs grown by MOCVD at high growth rates. *J. Phys. D Appl. Phys.* **2020**, *54*, 034005. [CrossRef]

105. Alema, F.; Zhang, Y.; Osinsky, A.; Valente, N.; Mauze, A.; Itoh, T.; Speck, J.S. Low temperature electron mobility exceeding 104 cm2/V s in MOCVD grown β-Ga_2O_3. *APL Mater.* **2019**, *7*, 121110. [CrossRef]
106. Chikoidze, E.; Sartel, C.; Madaci, I.; Mohamed, H.; Vilar, C.; Ballesteros, B.; Belarre, F.; del Corro, E.; Castro, P.V.; Sauthier, G.; et al. p-Type Ultrawide-Band-Gap Spinel ZnGa2O4: New Perspectives for Energy Electronics. *Cryst. Growth Des.* **2020**, *20*, 2535–2546. [CrossRef]
107. Chikoidze, E.; Rogers, D.; Teherani, F.; Rubio, C.; Sauthier, G.; Von Bardeleben, H.; Tchelidze, T.; Ton-That, C.; Fellous, A.; Bove, P.; et al. Puzzling robust 2D metallic conductivity in undoped β-Ga_2O_3 thin films. *Mater. Today Phys.* **2019**, *8*, 10–17. [CrossRef]
108. Perez-Tomas, A.; Lira-Cantu, M.; Catalan, G. Above-Bandgap Photovoltages in Antiferroelectrics. *Adv. Mater.* **2016**, *28*, 9644–9647. [CrossRef]
109. Pérez-Tomás, A. Functional Oxides for Photoneuromorphic Engineering: Toward a Solar Brain. *Adv. Mater. Interfaces* **2019**, *6*, 1900471. [CrossRef]
110. Chikoidze, E.; Von Bardeleben, H.J.; Akaiwa, K.; Shigematsu, E.; Kaneko, K.; Fujita, S.; Dumont, Y. Electrical, optical, and magnetic properties of Sn doped α-Ga_2O_3 thin films. *J. Appl. Phys.* **2016**, *120*, 025109. [CrossRef]
111. Guo, D.; Guo, Q.; Chen, Z.; Wu, Z.; Li, P.; Tang, W. Review of Ga_2O_3-based optoelectronic devices. *Mater. Today Phys.* **2019**, *11*, 100157. [CrossRef]
112. Goto, K.; Konishi, K.; Murakami, H.; Kumagai, Y.; Monemar, B.; Higashiwaki, M.; Kuramata, A.; Yamakoshi, S. Halide vapor phase epitaxy of Si doped β-Ga_2O_3 and its electrical properties. *Thin Solid Films* **2018**, *666*, 182–184. [CrossRef]
113. Yan, X.; Esqueda, I.S.; Ma, J.; Tice, J.; Wang, H. High breakdown electric field in β-Ga_2O_3/graphene vertical barristor heterostructure. *Appl. Phys. Lett.* **2018**, *112*, 032101. [CrossRef]
114. Chikoidze, E.; Fellous, A.; Perez-Tomas, A.; Sauthier, G.; Tchelidze, T.; Ton-That, C.; Huynh, T.T.; Phillips, M.; Russell, S.; Jennings, M.; et al. P-type β-gallium oxide: A new perspective for power and optoelectronic devices. *Mater. Today Phys.* **2017**, *3*, 118–126. [CrossRef]
115. Chikoidze, E.; Sartel, C.; Mohamed, H.; Madaci, I.; Tchelidze, T.; Modreanu, M.; Vales-Castro, P.; Rubio, C.; Arnold, C.; Sallet, V.; et al. Enhancing the intrinsic p-type conductivity of the ultra-wide bandgap Ga_2O_3 semiconductor. *J. Mater. Chem. C* **2019**, *7*, 10231–10239. [CrossRef]
116. Kyrtsos, A.; Matsubara, M.; Bellotti, E. On the feasibility of p-type Ga_2O_3. *Appl. Phys. Lett.* **2018**, *112*, 032108. [CrossRef]
117. Varley, J.B.; Janotti, A.; Franchini, C.; Van de Walle, C. Role of self-trapping in luminescence andp-type conductivity of wide-band-gap oxides. *Phys. Rev. B* **2012**, *85*, 081109. [CrossRef]
118. Lyons, J.L. A survey of acceptor dopants forβ-Ga_2O_3. *Semicond. Sci. Technol.* **2018**, *33*, 05LT02. [CrossRef]
119. Sun, D.; Gao, Y.; Xue, J.; Zhao, J. Defect stability and electronic structure of doped β-Ga_2O_3: A comprehensive ab initio study. *J. Alloys Compd.* **2019**, *794*, 374–384. [CrossRef]
120. Goyal, A.; Zakutayev, A.; Stevanović, V.; Lany, S. Computational Fermi level engineering and doping-type conversion of Mg:Ga_2O_3 via three-step synthesis process. *J. Appl. Phys.* **2021**, *129*, 245704. [CrossRef]
121. Sabino, F.P.; Cai, X.; Wei, S.-H.; Janotti, A. Bismuth-Doped Ga_2O_3 as Candidate for p-Type Transparent Conducting Material. *arXiv* **2019**, arXiv:190600840.
122. Li, L.; Liao, F.; Hu, X. The possibility of N–P codoping to realize P type β-Ga_2O_3. *Superlattices Microstruct.* **2020**, *141*, 106502. [CrossRef]
123. Ma, J.; Lin, J.; Liu, J.; Li, F.; Liu, Y.; Yang, G. Achieving high conductivity p-type Ga_2O_3 through Al-N and In-N co-doping. *Chem. Phys. Lett.* **2020**, *746*, 137308. [CrossRef]
124. Zhang, L.; Yan, J.; Zhang, Y.; Li, T.; Ding, X. A comparison of electronic structure and optical properties between N-doped β-Ga_2O_3 and N–Zn co-doped β-Ga_2O_3. *Phys. B Condens. Matter* **2012**, *407*, 1227–1231. [CrossRef]
125. Qian, Y.; Guo, D.; Chu, X.; Shi, H.; Zhu, W.; Wang, K.; Huang, X.; Wang, H.; Wang, S.; Li, P.; et al. Mg-doped p-type β-Ga_2O_3 thin film for solar-blind ultraviolet photodetector. *Mater. Lett.* **2017**, *209*, 558–561. [CrossRef]
126. Yue, W.; Yan, J.; Wu, J.; Zhang, L. Structural and optical properties of Zn-doped β-Ga_2O_3films. *J. Semicond.* **2012**, *33*, 073003. [CrossRef]
127. Alema, F.; Hertog, B.; Ledyaev, O.; Volovik, D.; Thoma, G.; Miller, R.; Osinsky, A.; Mukhopadhyay, P.; Bakhshi, S.; Ali, H.; et al. Solar blind photodetector based on epitaxial zinc doped Ga2 O3 thin film. *Phys. Status Solidi* **2017**, *214*, 1600688. [CrossRef]
128. Su, Y.; Guo, D.; Ye, J.; Zhao, H.; Wang, Z.; Wang, S.; Li, P.; Tang, W. Deep Level Acceptors of Zn-Mg Divalent Ions Dopants in b-Ga_2O_3 for the Difficulty to p-Type Conductivity. *J. Alloys Compd.* **2019**, *782*, 299–303. [CrossRef]
129. Feng, Q.; Liu, J.; Yang, Y.; Pan, D.; Xing, Y.; Shi, X.; Xia, X.; Liang, H. Catalytic growth and characterization of single crystalline Zn doped p-type β-Ga_2O_3 nanowires. *J. Alloys Compd.* **2016**, *687*, 964–968. [CrossRef]
130. Islam, M.; Liedke, M.O.; Winarski, D.; Butterling, M.; Wagner, A.; Hosemann, P.; Wang, Y.; Uberuaga, B.; Selim, F.A. Chemical manipulation of hydrogen induced high p-type and n-type conductivity in Ga_2O_3. *Sci. Rep.* **2020**, *10*, 6134. [CrossRef]
131. Wu, Z.; Jiang, Z.; Ma, C.; Ruan, W.; Chen, Y.; Zhang, H.; Zhang, G.; Fang, Z.; Kang, J.; Zhang, T.-Y. Energy-driven multi-step structural phase transition mechanism to achieve high-quality p-type nitrogen-doped β-Ga_2O_3 films. *Mater. Today Phys.* **2021**, *17*, 100356. [CrossRef]
132. Yao, Y.; Davis, R.F.; Porter, L.M. Investigation of different metals as ohmic contacts to β-Ga_2O_3: Comparison and analysis of electrical behavior, morphology, and other physical properties. *J. Electron. Mater.* **2017**, *46*, 2053–2060. [CrossRef]

133. Ji, M.; Taylor, N.R.; Kravchenko, I.; Joshi, P.; Aytug, T.; Cao, L.R.; Paranthaman, M.P. Demonstration of Large-Size Vertical Ga_2O_3 Schottky Barrier Diodes. *IEEE Trans. Power Electron.* **2020**, *36*, 41–44. [CrossRef]
134. Yao, Y.; Gangireddy, R.; Kim, J.; Das, K.K.; Davis, R.F.; Porter, L.M. Electrical behavior of β-Ga_2O_3 Schottky diodes with different Schottky metals. *J. Vac. Sci. Technol. B Nanotechnol. Microelectron. Mater. Process. Meas. Phenom.* **2017**, *35*, 03D113. [CrossRef]
135. Lu, X.; Zhou, L.; Chen, L.; Ouyang, X.; Tang, H.; Liu, B.; Xu, J. X-ray Detection Performance of Vertical Schottky Photodiodes Based on a Bulk β-Ga_2O_3 Substrate Grown by an EFG Method. *ECS J. Solid State Sci. Technol.* **2019**, *8*, Q3046–Q3049. [CrossRef]
136. Higashiwaki, M.; Konishi, K.; Sasaki, K.; Goto, K.; Nomura, K.; Thieu, Q.T.; Togashi, R.; Murakami, H.; Kumagai, Y.; Monemar, B.; et al. Temperature-dependent capacitance–voltage and current–voltage characteristics of Pt/Ga_2O_3 (001) Schottky barrier diodes fabricated on n^-–Ga_2O_3 drift layers grown by halide vapor phase epitaxy. *Appl. Phys. Lett.* **2016**, *108*, 133503. [CrossRef]
137. Harada, T.; Ito, S.; Tsukazaki, A. Electric Dipole Effect in $PdCoO_2$/β-Ga_2O_3 Schottky Diodes for High-Temperature Operation. *Sci. Adv.* **2019**, *5*, eaax5733. [CrossRef]
138. Pérez-Tomás, A.; Mingorance, A.; Tanenbaum, D.; Lira-Cantú, M. Chapter 8—Metal Oxides in Photovoltaics: All-Oxide, Ferroic, and Perovskite Solar Cells. In *The Future of Semiconductor Oxides in Next-Generation Solar Cells*; Lira-Cantu, M., Ed.; Elsevier: Amsterdam, The Netherlands, 2018; pp. 267–356.
139. Carey IV, P.H.; Yang, J.; Ren, R.; Sharma, R.; Law, M.; Pearton, S.J. Comparison of Dual-Stack Dielectric Field Plates on β-Ga_2O_3 Schottky Rectifiers. *ECS J. Solid State Sci. Technol.* **2019**, *8*, 7. [CrossRef]
140. Chen, Y.-T.; Yang, J.; Ren, F.; Chang, C.-W.; Lin, J.; Pearton, S.J.; Tadjer, M.J.; Kuramata, A.; Liao, Y.-T. Implementation of a 900 V Switching Circuit for High Breakdown Voltage β-Ga_2O_3 Schottky Diodes. *ECS J. Solid State Sci. Technol.* **2019**, *8*, 7. [CrossRef]
141. Hu, Z.; Zhou, H.; Feng, Q.; Zhang, J.; Zhang, C.; Dang, K.; Cai, Y.; Feng, Z.; Gao, Y.; Kang, X.; et al. Field-Plated Lateral β-Ga_2O_3 Schottky Barrier Diode with High Reverse Blocking Voltage of More Than 3 kV and High DC Power Figure-of-Merit of 500 MW/cm^2. *IEEE Electron Device Lett.* **2018**, *39*, 1564–1567. [CrossRef]
142. Hu, Z.; Zhou, H.; Dang, K.; Cai, Y.; Feng, Z.; Gao, Y.; Feng, Q.; Zhang, J.; Hao, Y. Lateral β -Ga_2O_3 Schottky Barrier Diode on Sapphire Substrate With Reverse Blocking Voltage of 1.7 kV. *IEEE J. Electron Devices Soc.* **2018**, *6*, 815–820. [CrossRef]
143. Oh, S.; Yang, G.; Kim, J. Electrical Characteristics of Vertical Ni/β-Ga_2O_3 Schottky Barrier Diodes at High Temperatures. *ECS J. Solid State Sci. Technol.* **2016**, *6*, Q3022. [CrossRef]
144. Müller, S.; Thyen, L.; Splith, D.; Reinhardt, A.; Wenckstern, H.V.; Grundmann, M. High-Quality Schottky Barrier Diodes on β-Gallium Oxide Thin Films on Glass Substrate. *ECS J. Solid State Sci. Technol* **2019**, *8*, Q3126. [CrossRef]
145. Tadjer, M.J.; Wheeler, V.D.; Shahin, D.I.; Eddy, C.R., Jr.; Kub, F.J. Thermionic Emission Analysis of TiN and Pt Schottky Contacts to β-Ga_2O_3. *ECS J. Solid State Sci. Technol.* **2017**, *6*, 4. [CrossRef]
146. Du, L.; Xin, Q.; Xu, M.; Liu, Y.; Mu, W.; Yan, S.; Wang, X.; Xin, G.; Jia, Z.; Tao, X.-T.; et al. High-Performance Ga_2O_3 Diode Based on Tin Oxide Schottky Contact. *IEEE Electron Device Lett.* **2019**, *40*, 451–454. [CrossRef]
147. Hu, Z.; Li, J.; Zhao, C.; Feng, Z.; Tian, X.; Zhang, Y.; Zhang, Y.; Ning, J.; Zhou, H.; Zhang, C.; et al. Design and Fabrication of Vertical Metal/TiO2/β-Ga_2O_3 Dielectric Heterojunction Diode With Reverse Blocking Voltage of 1010 V. *IEEE Trans. Electron Devices* **2020**, *67*, 5628–5632. [CrossRef]
148. Fontserè, A.; Pérez-Tomás, A.; Banu, V.; Godignon, P.; Millán, J.; de Vleeschouwer, H.; Parsey, J.M.; Moens, P. A HfO2 based 800V/300 °C Au-Free AlGaN/GaN-on-Si HEMT Technology. In Proceedings of the 2012 24th International Symposium on Power Semiconductor Devices and ICs, Bruges, Belgium, 3–7 June 2012; 2012; pp. 37–40.
149. Zhou, H.; Yan, Q.L.; Zhang, J.C.; Lv, Y.J.; Liu, Z.H.; Zhang, Y.N.; Dang, K.; Dong, P.F.; Feng, Z.Q.; Feng, Q.; et al. High-Performance Vertical β-Ga_2O_3 Schottky Barrier Diode With Implanted Edge Termination. *IEEE Electron Device Lett.* **2019**, *40*, 1788–1791. [CrossRef]
150. Lin, C.-H.; Yuda, Y.; Wong, M.H.; Sato, M.; Takekawa, N.; Konishi, K.; Watahiki, T.; Yamamuka, M.; Murakami, H.; Kumagai, Y.; et al. Vertical Ga_2O_3 Schottky Barrier Diodes With Guard Ring Formed by Nitrogen-Ion Implantation. *IEEE Electron Device Lett.* **2019**, *40*, 1487–1490. [CrossRef]
151. Wang, Y.G.; Lv, Y.J.; Long, S.B.; Zhou, X.Y.; Song, X.B.; Liang, S.L.; Han, T.T.; Tan, X.; Feng, Z.H.; Cai, S.J.; et al. High-Voltage (201) β-Ga_2O_3 Vertical Schottky Barrier Diode With Thermally-Oxidized Termination. *IEEE Electron Device Lett.* **2020**, *41*, 131–134. [CrossRef]
152. Allen, N.; Xiao, M.; Yan, X.; Sasaki, K.; Tadjer, M.J.; Ma, J.; Zhang, R.; Wang, H.; Zhang, Y. Vertical Ga_2O_3 Schottky Barrier Diodes With Small-Angle Beveled Field Plates: A Baliga's Figure-of-Merit of 0.6 GW/cm^2. *IEEE Electron Device Lett.* **2019**, *40*, 1399–1402. [CrossRef]
153. Li, W.S.; Nomoto, K.; Hu, Z.Y.; Jena, D.; Xing, H.L.G. Field-Plated Ga_2O_3 Trench Schottky Barrier Diodes With a BV2/$R_{on,sp}$ of up to 0.95 GW/cm^2. *IEEE Electron Device Lett.* **2020**, *41*, 107–110. [CrossRef]
154. Saitoh, Y.; Sumiyoshi, K.; Okada, M.; Horii, T.; Miyazaki, T.; Shiomi, H.; Ueno, M.; Katayama, K.; Kiyama, M.; Nakamura, T. Extremely Low On-Resistance and High Breakdown Voltage Observed in Vertical GaN Schottky Barrier Diodes with High-Mobility Drift Layers on Low-Dislocation-Density GaN Substrates. *Appl. Phys. Express* **2010**, *3*, 081001. [CrossRef]
155. Xiao, M.; Ma, Y.; Cheng, K.; Liu, K.; Xie, A.; Beam, E.; Cao, Y.; Zhang, Y. 3.3 kV Multi-Channel AlGaN/GaN Schottky Barrier Diodes With P-GaN Termination. *IEEE Electron Device Lett.* **2020**, *41*, 1177–1180. [CrossRef]
156. Kizilyalli, I.C.; Edwards, A.P.; Aktas, O.; Prunty, T.; Bour, D. Vertical Power p-n Diodes Based on Bulk GaN. *IEEE Trans. Electron Devices* **2014**, *62*, 414–422. [CrossRef]

157. Watahiki, T.; Yuda, Y.; Furukawa, A.; Yamamuka, M.; Takiguchi, Y.; Miyajima, S. Heterojunction p-Cu2O/n-Ga_2O_3 diode with high breakdown voltage. *Appl. Phys. Lett.* **2017**, *111*, 222104. [CrossRef]
158. Lu, X.; Zhou, X.; Jiang, H.; Ng, K.W.; Chen, Z.; Pei, Y.; Lau, K.M.; Wang, G. 1-kV Sputtered p-NiO/n-Ga_2O_3 Heterojunction Diodes with an Ultra-Low Leakage Current Below 1uA/cm2. *IEEE Electron Device Lett.* **2020**, *41*, 449–452. [CrossRef]
159. Gong, H.H.; Chen, X.H.; Xu, Y.; Ren, F.-F.; Gu, S.L.; Ye, J.D. A 1.86-kV Double-Layered NiO/β-Ga_2O_3 Vertical p–n Heterojunction Diode. *Appl. Phys. Lett.* **2020**, *117*, 022104. [CrossRef]
160. Pérez-Tomás, A.; Chikoidze, E.; Dumont, Y.; Jennings, M.R.; Russell, S.O.; Vales-Castro, P.; Catalan, G.; Lira-Cantú, M.; Ton–That, C.; Teherani, F.H.; et al. Giant Bulk Photovoltaic Effect in Solar Cell Architectures with Ultra-Wide Bandgap Ga_2O_3 Transparent Conducting Electrodes. *Mater. Today Energy* **2019**, *14*, 100350. [CrossRef]
161. Russell, S.A.O.; Jennings, M.R.; Dai, T.X.; Li, F.; Hamilton, D.P.; Fisher, C.A.; Sharma, Y.K.; Mawby, P.A.; Pérez-Tomás, A. Functional Oxide as an Extreme High-k Dielectric towards 4H-SiC MOSFET Incorporation. *Mater. Sci. Forum* **2017**, *897*, 155–158. [CrossRef]
162. Xia, Z.; Chandrasekar, H.; Moore, W.; Wang, C.; Lee, A.J.; McGlone, J.; Kalarickal, N.K.; Arehart, A.; Ringel, S.; Yang, F.; et al. Metal/$BaTiO_3$/β-Ga_2O_3 dielectric heterojunction diode with 5.7 MV/cm breakdown field. *Appl. Phys. Lett.* **2019**, *115*, 252104. [CrossRef]
163. Razzak, T.; Chandrasekar, H.; Hussain, K.; Lee, C.H.; Mamun, A.; Xue, H.; Xia, Z.; Sohel, S.H.; Rahman, M.W.; Bajaj, S.; et al. $BaTiO_3$/Al0.58Ga0.42N lateral heterojunction diodes with breakdown field exceeding 8 MV/cm. *Appl. Phys. Lett.* **2020**, *116*, 023507. [CrossRef]
164. Kalarickal, N.K.; Feng, Z.; Bhuiyan, A.; Xia, Z.; McGlone, J.F.; Moore, W.; Arehart, A.R.; Ringel, S.A.; Zhao, H.; Rajan, S. Electrostatic engineering using extreme permittivity materials for ultra-wide band gap semiconductor transistors. *arXiv* **2020**, arXiv:2006.02349.
165. Roy, S.; Bhattacharyya, A.; Krishnamoorthy, S. Analytical Modeling and Design of Gallium Oxide Schottky Barrier Diodes Beyond Unipolar Figure of Merit Using High-k Dielectric Superjunction Structures. *arXiv* **2020**, arXiv:2008.00280.
166. Pérez-Tomás, A.; Fontserè, A.; Jennings, M.R.; Gammon, P.M. Modeling the Effect of Thin Gate Insulators (SiO_2, SiN, Al_2O_3 and HfO2) on AlGaN/GaN HEMT Forward Characteristics Grown on Si, Sapphire and SiC. *Mater. Sci. Semicond. Processing* **2013**, *16*, 1336–1345. [CrossRef]
167. Sasaki, K.; Higashiwaki, M.; Kuramata, A.; Masui, T.; Yamakoshi, S. Si-Ion Implantation Doping in β-$Ga_2O_3$and Its Application to Fabrication of Low-Resistance Ohmic Contacts. *Appl. Phys. Express* **2013**, *6*, 086502. [CrossRef]
168. Zhou, H.; Si, M.; Alghamdi, S.; Qiu, G.; Yang, L.; Ye, P.D. High performance depletion/enhancement-mode β-Ga_2O_3 on insulator (GOOI) field-effect transistors with record drain currents of 600/450 mA/mm. *IEEE Electron Device Lett.* **2017**, *38*, 103–106. [CrossRef]
169. Carey, P.H., IV; Yang, J.; Ren, F.; Hays, D.C.; Pearton, S.J.; Jang, S.; Kuramata, A.; Kravchenko, I.I. Ohmic contacts on n-type β-Ga_2O_3 using AZO/Ti/Au. *AIP Adv.* **2017**, *7*, 095313. [CrossRef]
170. Fontserè, A.; Pérez-Tomás, A.; Placidi, M.; Fernández-Martínez, P.; Baron, N.; Chenot, S.; Cordier, Y.; Moreno, J.; Gammon, P.; Jennings, M. Temperature dependence of Al/Ti-based Ohmic contact to GaN devices: HEMT and MOSFET. *Microelectron. Eng.* **2011**, *88*, 3140–3144. [CrossRef]
171. Fontserè, A.; Pérez-Tomás, A.; Placidi, M.; Llobet, J.; Baron, N.; Chenot, S.; Cordier, Y.; Moreno, J.C.; Gammon, P.M.; Jennings, M.R.; et al. Micro and Nano Analysis of 0.2 Ω mm Ti/Al/Ni/Au Ohmic Contact to AlGaN/GaN. *Appl. Phys. Lett.* **2011**, *99*, 213504. [CrossRef]
172. Li, Z.; Liu, Y.; Zhang, A.; Liu, Q.; Shen, C.; Wu, F.; Xu, C.; Chen, M.; Fu, H.; Zhou, C. Quasi-two-dimensional β-Ga_2O_3 field effect transistors with large drain current density and low contact resistance via controlled formation of interfacial oxygen vacancies. *Nano Res.* **2018**, *12*, 143–148. [CrossRef]
173. Chabak, K.D.; McCandless, J.P.; Moser, N.A.; Green, A.J.; Mahalingam, K.; Crespo, A.; Hendricks, N.; Howe, B.M.; Tetlak, S.E.; Leedy, K.; et al. Recessed-gate enhancement-mode-Ga_2O_3 MOSFETs. *IEEE Electron Device Lett.* **2018**, *39*, 67–70. [CrossRef]
174. Hu, Z.; Nomoto, K.; Li, W.; Tanen, N.; Sasaki, K.; Kuramata, A.; Nakamura, T.; Jena, D.; Xing, H.G. Enhancement-Mode Ga_2O_3 Vertical Transistors With Breakdown Voltage >1 kV. *IEEE Electron Device Lett.* **2018**, *39*, 869–872. [CrossRef]
175. Hu, Z.; Nomoto, K.; Li, W.; Jinno, R.; Nakamura, T.; Jena, D.; Xing, H. 1.6 kV Vertical Ga_2O_3 FinFETs With Source-Connected Field Plates and Normally-off Operation. In Proceedings of the 31st International Symposium on Power Semiconductor Devices and ICs (ISPSD), Shanghai, China, 19–23 May 2019; 2019; pp. 483–486.
176. Li, W.; Nomoto, K.; Hu, Z.; Nakamura, T.; Jena, D.; Xing, H.G. Single and multi-fin normally-off Ga_2O_3 vertical transistors with a breakdown voltage over 2.6 kV. Proceedings of IEDM Technical Digest, San Francisco, CA, USA, 1–4 December 2019.
177. Lv, Y.; Zhou, X.; Long, S.; Song, X.; Wang, Y.; Liang, S.; He, Z.; Han, T.; Tan, X.; Feng, Z.; et al. Source-Field-Plated β-Ga_2O_3 MOSFET with Record Power Figure of Merit of 50.4 MW/cm^2. *IEEE Electron Device Lett.* **2019**, *40*, 83–86. [CrossRef]
178. Lv, Y.; Liu, H.; Zhou, X.; Wang, Y.; Song, X.; Cai, Y.; Yan, Q.; Wang, C.; Liang, S.; Zhang, J.; et al. Lateral β-Ga_2O_3 MOSFETs With High Power Figure of Merit of 277 MW/cm^2. *IEEE Electron Device Lett.* **2020**, *41*, 537–540. [CrossRef]
179. Tetzner, K.; Treidel, E.B.; Hilt, O.; Popp, A.; Anooz, S.B.; Wagner, G.; Thies, A.; Ickert, K.; Gargouri, H.; Würfl, J. Lateral 1.8 kV β-Ga_2O_3 MOSFET with 155 MW/cm^2 Power Figure of Merit. *IEEE Electron Device Lett.* **2019**, *40*, 1503–1506. [CrossRef]
180. Sharma, S.; Zeng, K.; Saha, S.; Singisetti, U. Field-plated lateral Ga_2O_3 MOSFETs with polymer passivation and 8.03 kV breakdown voltage. *IEEE Electron Device Lett.* **2020**, *41*, 836–839. [CrossRef]

181. Shibata, D.; Kajitani, R.; Ogawa, M.; Tanaka, K.; Tamura, S.; Hatsuda, T. 1.7 kV/1.0 mΩcm^2 normally-off vertical GaN transistor on GaN substrate with regrown p-GaN/AlGaN/GaN semipolar gate structure. Proceedings of IEDM Technical Digest, San Francisco, CA, USA, 1–4 December 2016.
182. Uemoto, Y.; Shibata, D.; Yanagihara, M.; Ishida, H.; Matsuo, H.; Nagai, S. 8300 V blocking voltage AlGaN/GaN power HFET with thick poly-AlN passivation. Proceedings of IEEE International Electron Devices Meeting, Washington, DC, USA, 10–12 December 2007; pp. 861–864.
183. Zhang, Y.; Neal, A.; Xia, Z.; Joishi, C.; Johnson, J.M.; Zheng, Y.; Bajaj, S.; Brenner, M.; Dorsey, D.; Chabak, K.; et al. Demonstration of high mobility and quantum transport in modulation-doped β-(AlxGa1-x)$_2$O$_3$/Ga$_2$O$_3$ heterostructures. *Appl. Phys. Lett.* **2018**, *112*, 173502. [CrossRef]
184. Song, K.; Zhang, H.; Fu, H.; Yang, C.; Singh, R.; Zhao, Y.; Sun, H.; Long, S. Normally-off AlN/β-Ga$_2$O$_3$ field-effect transistors using polarization-induced doping. *J. Phys. D Appl. Phys.* **2020**, *53*, 345107. [CrossRef]
185. Lyons, J.L. Electronic Properties of Ga$_2$O$_3$ Polymorphs. *ECS J. Solid State Sci. Technol.* **2019**, *8*, Q3226–Q3228. [CrossRef]
186. Roy, R.; Hill, V.G.; Osborn, E.F. Polymorphism of Ga$_2$O$_3$ and the System Ga$_2$O$_3$—H$_2$O. *J. Am. Chem. Soc.* **1952**, *74*, 719–722. [CrossRef]
187. Oshima, T.; Okuno, T.; Arai, N.; Kobayashi, Y.; Fujita, S. β-Al$_{2x}$Ga$_{2-2x}$O$_3$ Thin Film Growth by Molecular Beam Epitaxy. *Jpn. J. Appl. Phys.* **2009**, *48*, 070202. [CrossRef]
188. Jinno, R.; Chang, C.S.; Onuma, T.; Cho, Y.; Ho, S.-T.; Rowe, D.; Cao, M.C.; Lee, K.; Protasenko, V.; Schlom, D.G.; et al. Crystal orientation dictated epitaxy of ultrawide-bandgap 5.4- to 8.6-eV α-(AlGa)$_2$O$_3$ on m-plane sapphire. *Sci. Adv.* **2021**, *7*, eabd5891. [CrossRef] [PubMed]
189. Jinno, R.; Kaneko, K.; Fujita, S. Thermal stability of α-(Al$_x$Ga$_{1-x}$)$_2$O$_3$ films grown on c-plane sapphire substrates with an Al composition up to 90%. *Jpn. J. Appl. Phys.* **2021**, *60*, SBBD13. [CrossRef]
190. Chi, Z.; Tarntair, F.-G.; Frégnaux, M.; Wu, W.-Y.; Sartel, C.; Madaci, I.; Chapon, P.; Sallet, V.; Dumont, Y.; Pérez-Tomás, A.; et al. Bipolar Self-doping in Ultra-wide Bandgap Spinel ZnGa$_2$O$_4$. *Mater. Today Phys.* **2021**, *20*, 100466. [CrossRef]
191. Chen, M.-I.; Singh, A.; Chiang, J.-L.; Horng, R.-H.; Wuu, D.-S. Zinc Gallium Oxide—A Review from Synthesis to Applications. *Nanomaterials* **2020**, *10*, 2208. [CrossRef]
192. Galazka, Z.; Irmscher, K.; Pietsch, M.; Ganschow, S.; Schulz, D.; Klimm, D.; Hanke, I.M.; Schroeder, T.; Bickermann, M. Experimental Hall electron mobility of bulk single crystals of transparent semiconducting oxides. *J. Mater. Res.* **2021**, *36*, 4746–4755. [CrossRef]
193. Galazka, Z.; Klimm, D.; Irmscher, K.; Uecker, R.; Pietsch, M.; Bertram, R.; Naumann, M.; Albrecht, M.; Kwasniewski, A.; Schewski, R.; et al. MgGa$_2$O$_4$ as a new wide bandgap transparent semiconducting oxide: Growth and properties of bulk single crystals. *Phys. Status Solidi* **2015**, *212*, 1455–1460. [CrossRef]